JOURNAL OF PETROLOGY | VOLUME 51 | NUMBER 4 | PAGES 785–821 | 2010 | doi:10.1093/petrology/egp095

Mechanisms of Crustal Anatexis: a Geochemical Study of Partially Melted Metapelitic Enclaves and Host Dacite, SE Spain

ANTONIO ACOSTA-VIGIL[1]*, IAN BUICK[2], JÖRG HERMANN[3], BERNARDO CESARE[4], DANIELA RUBATTO[3], DAVID LONDON[5] AND GEORGE B. MORGAN, VI[5]

[1]INSTITUTO ANDALUZ DE CIENCIAS DE LA TIERRA, CONSEJO SUPERIOR DE INVESTIGACIONES CIENTÍFICAS, 18002 GRANADA, SPAIN

[2]DEPARTMENT OF GEOLOGY, GEOGRAPHY AND ENVIRONMENTAL STUDIES, STELLENBOSCH UNIVERSITY, MATIELAND, 7602 STELLENBOSCH, SOUTH AFRICA

[3]RESEARCH SCHOOL OF EARTH SCIENCES, THE AUSTRALIAN NATIONAL UNIVERSITY, CANBERRA ACT 0200, AUSTRALIA

[4]DIPARTIMENTO DI GEOSCIENZE, UNIVERSITÀ DI PADOVA, 35137 PADOVA, ITALY

[5]SCHOOL OF GEOLOGY AND GEOPHYSICS, UNIVERSITY OF OKLAHOMA, NORMAN, OK 73019, USA

RECEIVED AUGUST 3, 2009; ACCEPTED DECEMBER 14, 2009
ADVANCE ACCESS PUBLICATION FEBRUARY 6, 2010

To shed light on the mechanisms of crustal anatexis, a detailed geochemical study has been conducted on minerals and glasses of quenched anatectic metapelitic enclaves and their host peraluminous dacites at El Hoyazo, SE Spain. Anatectic enclaves, composed of plagioclase + biotite + sillimanite + garnet + glass ± K-feldspar ± cordierite + graphite, formed during the rapid heating and overstepped melting of a greenschist-facies metapelite, and finally equilibrated at 850 ± 50°C and 5–7 kbar. Glass appears as melt inclusions within all mineral phases and in the matrix of the enclaves, and has a major element composition similar to that of peraluminous leucogranites. Melt inclusions and matrix glasses have normative quartz–orthoclase–albite compositions that plot in the vicinity of H_2O-undersaturated haplogranite eutectics. Melt inclusions show some compositional variability, with high Li, Cs and B, low Y, first row transition elements (FRTE) and rare earth elements (REE), and zircon and monazite saturation temperatures of ~665–750°C. They are interpreted as melts produced by muscovite-breakdown melting reactions at the onset of the process of rapid melting and mostly under H_2O-undersaturated conditions. Compared with melt inclusions, matrix glasses show less compositional variability, lower large ion lithophile element contents, higher Y, FRTE and REE, and higher zircon and monazite saturation temperatures (~695–815°C). They are interpreted as former melts recording the onset of biotite dehydration-melting. Matrix glasses in the dacite are compositionally different from glasses in the enclaves, hence the genetic connection between metasedimentary enclaves and dacite is not as straightforward as previous petrographic and bulk major element data suggest; this opens the possibility for some alternative interpretation. This study shows the following: (1) melt inclusions provide a window of information into the prograde evolution of anatexis in the enclaves; (2) melting occurred for the most part under H_2O-undersaturated conditions even if, because of the rapid heating, the protolith preserved most of the structurally bound H_2O contained at greenschist facies up to the beginning of anatexis, such that the excess H_2O maximized the amount of H_2O-undersaturated melt generated during anatexis; (3) although a large proportion of accessory minerals are currently shielded within major mineral phases, they have progressively dissolved to a considerable extent into the melt phase along the prograde anatectic path, as indicated by the relative clustering of accessory mineral saturation temperatures and closeness of these temperatures to those of potential melting reactions; (4) the dacite magma was probably produced by coalescence of melts

*Corresponding author. E-mail: aacosta@ugr.es

derived from several compositionally distinct metasedimentary protoliths.

KEY WORDS: *crustal anatexis; geochemistry; LA-ICP-MS; melt inclusions; metapelitic enclaves; granite; melting models*

INTRODUCTION

Crustal anatexis, accompanied by melt extraction and ascent of magma to upper crustal levels, constitutes the most important mechanism of geochemical differentiation of the continental crust (e.g. Vielzeuf *et al.*, 1990). Hence knowledge of the mechanisms and kinetics of anatexis, as well as of the processes of magma segregation, accumulation and transfer, is essential for characterizing the internal differentiation of the Earth's crust and the relationships between crustal granites and their source areas (e.g. Sawyer, 1991, 1994; Brown *et al.*, 1995; Bea, 1996*a*; Acosta-Vigil *et al.*, 2006). The study of anatectic terranes provides important information on the reactions and P–T conditions that generate crustal melts. However, complex reaction histories along the prograde path and slow cooling rates during the retrograde path prevent anatectic terranes from yielding a detailed characterization of the melt chemistry and residue–melt microstructural and geochemical relationships (e.g. Brown, 2002). This problem can potentially be overcome by the study of anatectic enclaves within volcanic rocks. The rapid ascent and extrusion of the enclaves within the host magma quench the melt phase to glass and freeze the microstructural and geochemical relationships between melt and residue at a given stage of anatexis (see Cesare, 2008). Of particular interest are those enclaves that are genetically related to their host volcanic rocks, because the detailed study of volcanic rocks and enclaves may provide direct observation of the process of genesis of crustal granitoid melts and valuable information on the geochemical relationships between crustal granites and source areas (see also Miller *et al.*, 1992).

The El Hoyazo dacite and included crustal anatectic enclaves were interpreted by Zeck (1968, 1970, 1992) as an erupted anatectic melt containing abundant residual material; hence, it potentially represents an extremely important natural scenario for the study of the different aspects of crustal anatexis (see also Cesare *et al.*, 1997). Careful field observations, petrographic work and geochemical analyses have provided a general framework for understanding the petrogenesis of the dacite (Zeck, 1968, 1970, 1992; Munksgaard, 1984; Zeck & Williams, 2002). More recently, Cesare and coworkers have described and started to characterize the widespread occurrence of glass (former silicate melt) as well as the presence and nature of fluid inclusions in the enclaves. Combined with detailed microstructural and analytical work on the enclaves, and isotopic analyses from both enclaves and host dacite, these datasets have been used to unravel many details of the nature of crustal anatexis at El Hoyazo (Cesare, 2008; and references therein).

This study focuses on the mechanisms and kinetics of crustal anatexis from the comparison of experimental results (e.g. Tuttle & Bowen, 1958; Vielzeuf & Holloway, 1988; Acosta-Vigil *et al.*, 2006) with detailed microstructural and analytical [electron microprobe (EMP), LA-ICP-MS) data on glasses and minerals from crustal anatectic enclaves and their host peraluminous dacites (Acosta-Vigil *et al.*, 2007) in the Neogene Volcanic Province (NVP) of SE Spain. Previous studies have shown that glasses in primary melt inclusions and the matrix of some enclaves (the Grt–Bt–Sil type, see below; mineral abbreviations after Kretz, 1983) have weak to moderate peraluminous leucogranitic compositions (Acosta-Vigil *et al.*, 2007; see also Cesare *et al.*, 1997). Despite being leucogranitic, the glasses show some compositional variation correlated with their microstructural location, which seems to largely reflect the evolution of the bulk melt composition during prograde anatexis. Quartz–orthoclase–albite normative compositions close to the H_2O-undersaturated haplogranite eutectics, low (although minima) H_2O concentrations (calculated by difference between 100 and EMP totals), and low to moderate aluminium saturation index [ASI = mol. Al_2O_3/($CaO + Na_2O + K_2O$)] values of glasses, all strongly suggest melting under H_2O-undersaturated conditions (Acosta-Vigil *et al.*, 2007). However, the major element compositions do not seem to furnish any further information on the mechanisms of melting. This study complements that of Acosta-Vigil *et al.* (2007) and provides the trace element composition of minerals and glasses in Grt–Bt–Sil enclaves (the most common enclave type) and host dacite. This large volume of detailed geochemical data on clearly distingishable melt and solid phases provides important clues on the mechanisms of anatexis and it also raises some new questions. The present study (1) evaluates the significance of the compositional information provided by a large population of analyzed primary melt inclusions, (2) extracts the information on melt-forming reactions, fluid regime, and behavior and role of accessory phases during anatexis of the metapelitic enclaves, and (3) examines two interrelated questions about the age of partial melting in the enclaves and the relationships between enclaves and dacite, with several working hypotheses. A forthcoming paper uses this dataset to describe the state of equilibrium between the melt and the solid assemblage of the enclaves, the nature of trace element partitioning during crustal melting, and the consequences for crustal differentiation and the relationships between granites and their source areas.

GEOLOGICAL AND PETROLOGICAL SETTING

The El Hoyazo dacites (~6·33 ± 0·15 Ma, Zeck & Williams, 2002) form a small (~1 km diameter) volcano located within the NVP. Volcanism in the NVP is mostly late orogenic (~12–2 Ma, Duggen *et al.*, 2005; and references therein) with respect to peak metamorphism of the Betic Cordilleras, and occurred in an extensional setting (Fig. 1). The volcano comprises strongly peraluminous cordierite-bearing dacites, which host very abundant (20–25 vol. %) enclaves of predominantly anatectic metapelites (~10–15 vol. %) together with mafic, gabbroic to basaltic and dioritic material (~10 vol. %) (Zeck, 1992; Zeck & Williams, 2002). The metasedimentary enclaves have been classified into three main petrographic types: Grt–Bt–Sil, Spl–Crd and Qtz–Crd (Zeck, 1970, 1992). Based on the phase assemblage, microstructures, residual nature of bulk-rock major element composition and geothermobarometric calculations, the enclaves have been interpreted as residual material after partial melting and melt extraction (Zeck, 1970, 1992; Cesare *et al.*, 1997; Benito *et al.*, 1999). Several hypotheses have been proposed for the relationships between metapelitic enclaves and host dacite (Zeck, 1970; Benito *et al.*, 1999, and references therein; Duggen *et al.*, 2005). However, those studies focused primarily on the petrogenesis of the El Hoyazo dacites have interpreted these rocks to be a largely crustal magma produced by the partial melting of a metasedimentary protolith (Zeck, 1970, 1992; Cesare *et al.*, 1997, 2009*a*). According to this hypothesis, the residue left after partial melting and melt extraction is now represented by the anatectic metapelitic enclaves.

Garnet–Bt–Sil enclaves are composed of Pl + Bt + Sil + Grt + glass ± Kfs ± Crd + Gr + Ilm + Ap + Zrn + Mnz ± Spl (Cesare *et al.*, 1997, 2003). They represent fragments of a metapelitic continental crust with phase assemblages and compositions that record an earlier and major syn-deformation melting event at 850 ± 50°C and 5–7 kbar, followed by some other, (much) less complete and static equilibration stages of about equal to slightly higher T and lower P, such as 790–825°C at 5 kbar, 900–950°C at 5 kbar, and 820 ± 50°C at 4·5 ± 0·6 kbar (Cesare *et al.*, 1997; Cesare, 2000; Cesare & Gómez-Pugnaire, 2001; Álvarez-Valero *et al.*, 2005, 2007; Tajcmanová *et al.*, 2009). The earlier event is interpreted as a regional-scale process, whereas the later lower-pressure events have been interpreted as partial re-equilibration of the enclaves already in the dacitic magma, during ascent and residence of the latter at shallower crustal level(s) and before final eruption. A melt phase has been described as a product in reactions taking place during each of the above equilibration stages, hence melting reactions in the enclaves began in a regional metamorphic setting and continued in the more local environment represented by the dacite magma (Cesare *et al.*, 1997; Cesare & Gómez-Pugnaire, 2001;

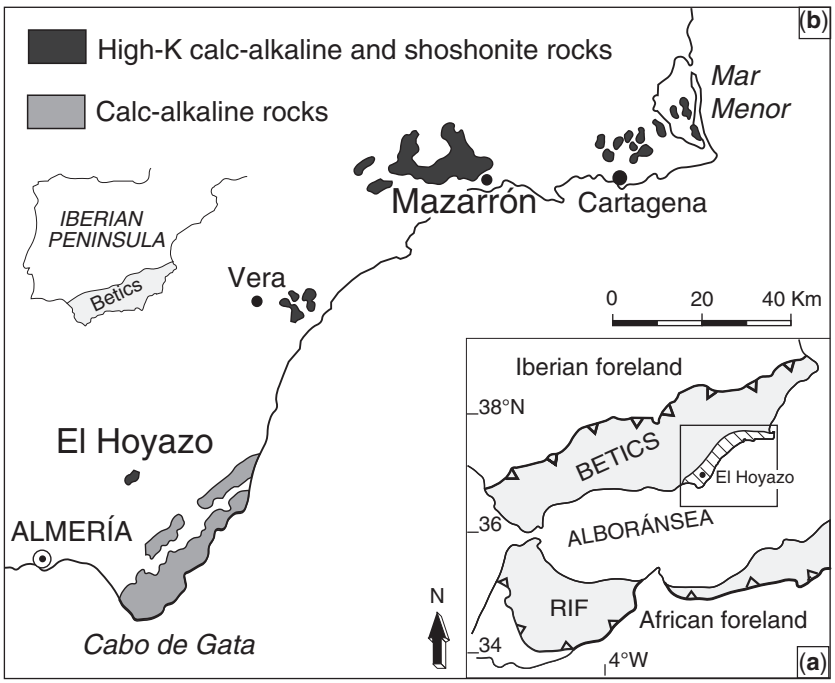

Fig. 1. Geographical location of (a) the Betic Cordillera (Betics) and Rif orogenic belts and (b) the volcanic rocks of the Neogene Volcanic Province of southeastern Spain (after López Ruiz & Rodríguez Badiola, 1980).

Álvarez-Valero *et al.*, 2005, 2007). Nevertheless, the above P–T estimates for the enclaves record only that part of the P–T–t history close to the thermal maximum, when the rocks were at temperatures far in excess of the wet pelite solidus. Hence the mineral major element compositional information about the subsolidus or lower-temperature suprasolidus segment of the P–T–t path has apparently been lost.

Cesare *et al.* (1997) and Cesare & Maineri (1999) noticed that glass associated with the regional metamorphic melting event appears in the matrix of the rock and as primary melt inclusions within all mineral phases, whether reactants or products of typical melting reactions in pelites. Cesare & Maineri (1999) hypothesized that the widespread presence of melt inclusions was due to the (re-)crystallization of all minerals in the presence of melt, during the process of rapid disequilibrium melting of a low-grade phyllite that equilibrated mineralogically to granulite-facies conditions, possibly bypassing most amphibolite-facies reactions. Thus they proposed the melting reaction

$$\mathrm{Chl} + \mathrm{Ms} + \mathrm{Qtz} + \mathrm{Ilm} + \mathrm{GCOH\ fluid}\ (\pm\mathrm{St} \pm \mathrm{Kfs} \pm \mathrm{Ky}) = \mathrm{Grt} + \mathrm{Pl} + \mathrm{Sil} + \mathrm{Bt} + \mathrm{melt} + \mathrm{Gr} \quad (1)$$

where 'GCOH fluid' stands for a mixture of H_2O, CO_2, CH_4, CO and H_2. They noticed that the reaction products appear equilibrated from a mineralogical and chemical point of view, and that the term 'disequilibrium melting' was used to reflect the presence of the original reactant assemblage (low-grade phyllite) outside its stability field. The presence of leucogranitic glass (former melt) as primary melt inclusions within all minerals and in the matrix of the enclaves demonstrates that (1) virtually all mineral phases (re-)crystallized in the presence of melt, hence (2) partial melting of the enclaves took place at depth, and (3) enclaves were brought to the surface rapidly within the host dacite magma while they still were in a partially molten state (Cesare *et al.*, 1997, 2003; Acosta-Vigil *et al.*, 2007).

PETROGRAPHY AND GEOCHEMISTRY

Garnet–Bt–Sil enclaves are the focus of this study, and consist primarily of plagioclase, biotite, sillimanite, garnet, silicate glass, alkali feldspar, cordierite and graphite. Quartz is rare, and newly crystallized alkali feldspar and plagioclase occur as quench products in the matrix glass. Common accessory phases include ilmenite, spinel, apatite, zircon and monazite (see Table 1 for weight proportions and compositional features; after Cesare *et al.*, 1997, 2003, 2005; and this study). Rare Th orthosilicates, allanite, barite, pyrite and Fe–Ni arsenates are also present. Silicate glass is present as melt inclusions within virtually all of the mineral phases and in the matrix of the enclaves (Fig. 2a–c). It has a peraluminous leucogranitic composition (SiO_2 ~70–73 wt %, FeO_t + MgO + TiO_2 ~1·4–1·9 wt %, ASI ~1·11–1·22). Plagioclase is anhedral, variable in grain size (~0·1–2 cm) and commonly elongated parallel to the foliation. Sillimanite is fibrolitic and is commonly (always?) intimately intergrown with glass (the 'mix' of Cesare, 2000). Garnet is subhedral to euhedral and ~0·1–0·5 cm in diameter. Alkali feldspar is anhedral and is commonly included within, or intergrown with, large Pl crystals. It also locally forms rims a few hundred micrometers thick that separate (and replace?) residual Pl from matrix glass (Fig. 2c). Quartz is present as common minute inclusions shielded within Pl, Grt and Crd, and as rare millimeter-sized rounded grains in the matrix in contact with glass. Enclaves display a well-developed foliation defined by sillimanite folia, abundant graphite, and the alternation of biotite- and plagioclase-rich layers. The foliation anastomoses around garnet porphyroblasts and nodular pseudomorphs of fibrolitic sillimanite intergrown with glass, which appear to replace garnet. Cordierite is rare and appears as centimeter-sized patchy poikiloblasts. It is generally devoid of melt inclusions and seems to postdate the development of the foliation defined by the main mineral assemblage Grt + Pl + Sil + Bt + melt. Matrix glass is in contact with all mineral phases and appears as films hundreds of microns to millimeters thick parallel to the foliation, as rounded pods, in strain shadows, or as

Table 1: Calculated modal abundances of phases in enclave HO-50 (see text for details)

Phase	wt %	Compositional features
Pl res	37·2	An_{25-35}
Bt	20·3	Mg-no. = 0·33–0·35
Sil	12·9	
Grt	11·8	Mg-no. = 0·12–0·15
Glass	11	
Kfs res	2·8	Or_{77-71}
Gr	1	
Kfs + Pl new	1	
Crd	0·2	Mg-no. = 0·50–0·55
Ilm	1·2	
Ap	0·5	
Zrn	0·1	
Mnz	0·03	
Th orthosilicates	0·0001	

Mineral abbreviations after Kretz (1983). 'res', residual; 'new', newly crystallized from the melt. Mg-number = molar [MgO/(MgO + FeO_t)].

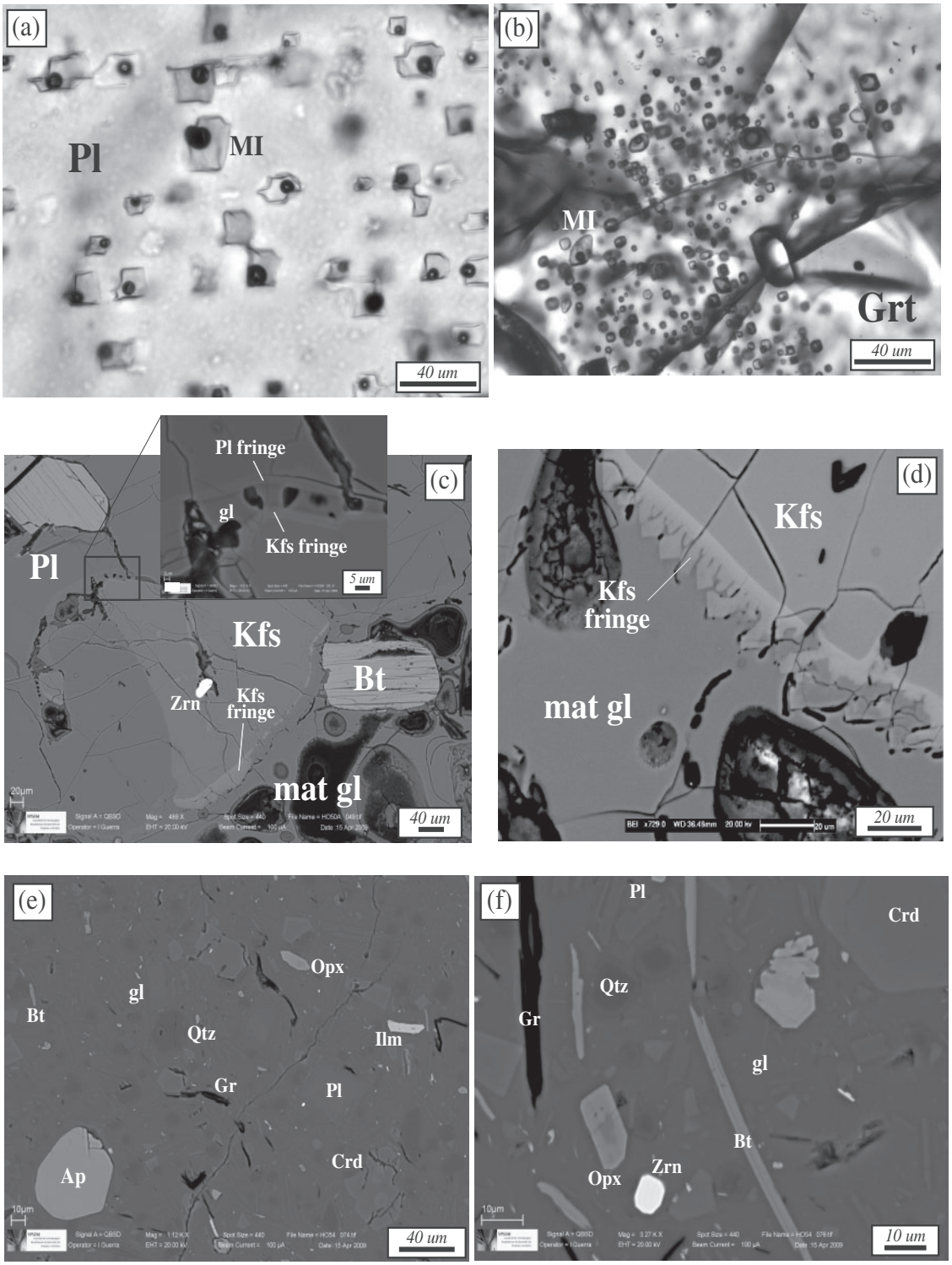

Fig. 2. Petrographic microscope and backscattered electron (BSE) images of Grt–Bt–Sil enclaves and El Hoyazo dacite. Mineral abbreviations are after Kretz (1983); MI, melt inclusion; gl, glass; mat gl, matrix glass. (a) Pl in Grt–Bt–Sil enclave crowded with MI; optical microscope, plane-polarized light (PPL). (b) MI in Grt of Grt–Bt–Sil enclave; optical microscope, PPL. (c) K-feldspar at the contact between Pl and matrix glass in Grt–Bt–Sil enclave; BSE image. K-feldspar and Pl fringes develop at the contact between Kfs–matrix glass and Pl–matrix glass, respectively (see the inset, corresponding to a detail of the upper left corner of the figure). (d) Detail of an ~10–20 μm thick Kfs fringe at the contact between residual Kfs and matrix glass in a Grt–Bt–Sil enclave; BSE image. (e, f) BSE images of El Hoyazo dacite showing euhedral Qtz, Pl, Bt, Crd and Opx microlites and accessory minerals Ap, Ilm and Zrn in the glassy matrix.

thin films around Grt. It has partially crystallized to feldspars, forming either skeletal to prismatic microlites or fringes nucleated on residual Pl and Kfs (Fig. 2c). Feldspar fringes frequently show skeletal microstructures, indicative of growth during quenching upon extrusion (Fig. 2d). Some melt inclusions in Pl also crystallize daughter feldspars. Evidence for syntectonic melting includes the foliation anastomosing around melt inclusion-bearing garnet porphyroblasts, deflection of biotite crystals containing melt inclusions and the presence of matrix glass in strain shadows or along thin foliation-parallel layers. This implies that melt inclusions and at least part of the matrix glasses were generated in the regional metamorphic setting (Cesare *et al.*, 1997, 2003; Cesare & Maineri, 1999; Cesare, 2000; Cesare & Gómez-Pugnaire, 2001; Acosta-Vigil *et al.*, 2007; and the present study).

The host dacite has a seriate microstructure and a glass-rich (~50 vol. %) groundmass. The phenocryst assemblage consists of euhedral crystals of plagioclase (~10 vol. %), cordierite (~9 vol. %), biotite (~8 vol. %) and small amounts of sillimanite, zircon and apatite. Plagioclase shows complex microstructures. The smaller crystals (~0·1–0·5 mm) have euhedral to subhedral oscillatory-zoned calcic cores ($An_{90–75}$), sharply overgrown by more sodic euhedral rims ($An_{60–40}$). Larger crystals (~0·5–1·5 mm) show, in addition, subhedral to anhedral sieve-textured and patchily zoned large core domains. Cordierite phenocrysts (~0·1–0·5 mm) commonly show transformation sector trillings, include acicular crystals of sillimanite arranged concentrically to the external euhedral shape, and show weak oscillatory zoning in Mg-number (~0·46–0·64) (Zeck, 1970, 1992; I. S. Buick *et al.*, unpublished data; J. M. Fernández-Soler *et al.*, unpublished data). The dacite also contains abundant xenocrysts of almandine-rich garnet, cordierite, quartz, plagioclase, spinel, graphite, zircon, orthopyroxene and hornblende (Zeck, 1970, 1992). Garnet xenocrysts are similar in shape, size, inclusions, major element zoning patterns and trace element composition to those in Grt–Bt–Sil enclaves (Zeck, 1970; Munksgaard, 1984; Table 2). Large anhedral cordierite grains, commonly in mineral aggregates with Bt + Sil + Ilm ± Gr ± Pl ± Grt ± Qtz, are microstructurally and compositionally similar to Crd in Grt–Bt–Sil enclaves and distinct from phenocrystic cordierite (Zeck, 1970; I. S. Buick *et al.*, unpublished data). Quartz is anhedral and embayed and apparently has been corroded by the dacite magma. Hornblende crystals are surrounded by Bt reaction rims (Zeck, 1970). Detailed scanning electron microscope (SEM) analysis also identified abundant Pl, Crd, Bt and Qtz, common Opx and scarce Als, as euhedral microlites ~5–30 μm in size grown from the melt (Fig. 2e and f; see below). In addition, the accessory mineral assemblage of the dacite includes ilmenite, apatite, zircon and monazite, with rare hercynitic spinel, chalcopyrite and chromite (see below). Whole-rock major element analyses of the matrix dacite (avoiding enclaves and centimeter-sized xenocrysts) are comparable with metapelite averages (Gromet *et al.*, 1984; Taylor & McLennan, 1985; e.g. Al_2O_3 ~16·9 wt %, Fe_2O_3 ~5·1 wt %, MgO ~1·9 wt %, K_2O ~3·3 wt %) except for somewhat lower ASI values (~1·46) and slightly higher CaO (~2·7 wt %) and Na_2O (~1·9 wt %) concentrations (Fernández-Soler *et al.*, 2007; see also Cesare *et al.*, 1997; Benito *et al.*, 1999).

METHODS

All analyses were performed on thin sections from two typical and previously well-characterized Grt–Bt–Sil enclaves (HO-33 and HO-50, Cesare *et al.*, 1997, 2003, 2005, 2009*a*; Acosta-Vigil *et al.*, 2007; Perini *et al.*, 2009) and a representative dacite sample (HO-54). Prior to analysis, all the samples were carefully characterized using conventional microscope petrography and CamScan MX2500 and LEO 1430-VP scanning electron microscopes at the Dipartimento di Geoscienze (Universitá di Padova) and Centro de Instrumentación Científica (Universidad de Granada), respectively.

In situ trace element analyses were performed by LA-ICP-MS at the Research School of Earth Sciences (Australian National University, ANU). A pulsed 193 nm ArF Excimer laser with 100 mJ energy at a repetition rate of 5 Hz coupled to an Agilent 7500 quadrupole ICP–MS system was used for ablation (Eggins *et al.*, 1998). Analyses were conducted on all minerals in the Grt–Bt–Sil enclaves, on silicate glasses found in the matrix of enclaves and as melt inclusions within Pl and Grt, and also on most minerals and matrix glass of the host dacite. Target areas for LA-ICP-MS analyses were previously identified from backscattered electron (BSE) images. Glasses within melt inclusions, the accessory phases Zrn, Mnz and Ilm, and newly crystallized feldspar fringes and microlites were analyzed with 19 and 40 μm beam diameters, whereas analyses on matrix glasses and all other mineral phases were performed using 40, 70 and 142 μm spots. The analyses on matrix glasses of dacite samples were conducted with a beam diamenter of 142 μm and included matrix glass plus microlites, mainly of Pl, Qtz, Crd and Bt; the uniformity of replicate analyses shows that phenocrysts and xenocrysts were successfully avoided. During the time-resolved analysis of minerals, possible contamination from inclusions and fractures was detected by monitoring several elements and integrating only the 'clean' part of the signal. The glasses NIST-612 (Pearce *et al.*, 1997) and BCR-2G (Norman *et al.*, 1998) were employed as external and secondary standards, respectively. The reproducibility of trace element results for the BCR glasses using the ANU analytical protocols are between 0·5% and 4% relative (1σ) for the majority of elements (Table 2), as discussed by

Table 2: Mean LA-ICP-MS analyses of silicate glasses and mineral phases at El Hoyazo, and BCR-2G and bulk-rock HO-50 trace element compositions

Material:	BCR-2G*	BCR-2G†	BCR-2G‡	MI in Pl	MI in Pl	MI in Grt	MI in Grt	Matrix gl	Matrix gl	Matrix gl
Enclave:	n.a.	n.a.	n.a.	HO-50A	HO-33A	HO-50A	HO-33A	HO-50A	HO-33A	HO-54
No. analyses:	1	1	19–26	18–22	2	2–20	8–12	20–28	2–11	39–48
SiO_2 (wt %)				67·14 (3·54)	63·97	66·61 (2·96)	72·74 (6·96)	68·04 (1·87)	66·07 (1·58)	68·00 (std)
Al_2O_3				12·87 (std)	13·51 (std)	14·55 (std)	14·45 (std)	13·99 (std)	14·48 (std)	15·00 (1·14)
CaO				0·22 (0·10)	0·42	0·73 (0·05)	0·66 (0·14)	0·40 (0·05)	0·43 (0·02)	1·36 (0·33)
P (ppm)			2080 (80)	n.d.	n.d.	1890 (140)	n.d.	1270 (200)	3660 (420)	990 (113)
Li	9·6		8·9 (0·7)	203 (291)	212	114 (121)	276 (90)	110 (46)	128 (34)	22 (3)
Rb	48·1	49	47 (3)	212 (24)	164	211 (11)	237 (30)	211 (24)	245 (11)	172 (14)
Cs	1·18	1·13	1·1 (0·1)	31 (4)	20	31 (8)	31 (4)	26 (4)	25 (3)	16 (1)
Be			2·0 (0·2)	2·4 (0·7)	2·3	2·7 (0·6)	2·5 (0·9)	0·87 (0·41)	1·4 (0·3)	2·1 (0·6)
B			5·6 (1·7)	329 (104)	207	185 (61)	449 (136)	196 (32)	149 (9)	151 (10)
Sr	335	342	300 (7)	28 (28)	28	165 (10)	112 (16)	82 (30)	34 (3)	196 (35)
Ba	672	660	609 (19)	79·7 (68·9)	50·4	308 (64)	235 (39)	355 (166)	199 (31)	469 (61)
Sc	33·5	33	32 (1)	n.d.	n.d.	2·0 (0·5)	n.d.	6·2 (1·8)	11 (1)	11 (3)
Ti	1·38	1·37	1·3 (0·5)	284 (250)	463	541 (185)	576 (27)	854 (476)	1280 (190)	1630 (690)
V	429		339 (16)	0·72 (0·44)	1·6	0·52 (0·57)	0·16 (0·10)	2·3 (0·9)	1·5 (0·2)	36 (28)
Cr			17 (1)	n.d.	n.d.	b.d.l.	n.d.	2·2 (0·8)	3·3 (1·4)	36 (20)
Co	38	35·8	35 (2)	n.d.	n.d.	n.d.	n.d.	0·89 (0·25)	1·2 (0·1)	5·0 (2·5)
Ni	13·3	10·8	11 (1)	n.d.	n.d.	n.d.	n.d.	0·34 (0·32)	0·58 (0·30)	8·2 (5·6)
Cu	34·1	19·4	14 (1)	n.d.	n.d.	n.d.	n.d.	4·7 (1·5)	3·5 (0·01)	8·2 (2·4)
Zn	129	147	144 (12)	54 (28)	48	60 (3)	53 (5)	34 (4)	39 (2)	56 (22)
As			1·1 (0·2)	91 (23)	39	82 (10)	96 (8)	55 (7)	52 (7)	53 (6·8)
Y	39·4	35·3	29 (1)	6·2 (1·9)	8·5	3·5 (1·4)	3·1 (2·7)	8·6 (3·1)	20 (3)	18 (1·2)
Zr	201	194	148 (6)	24 (8)	26	32 (6·6)	28 (1·3)	37 (6)	63 (7)	76 (7)
Hf	4·9	5	4·0 (0·2)	n.d.	n.d.	0·94 (0·21)	n.d.	1·1 (0·2)	1·6 (0·2)	2·5 (0·2)
Nb	13·1	12·8	11 (0)	9·3 (2·7)	7·3	12 (3)	16 (5)	9·3 (1·6)	8·9 (0·5)	13 (3)
Ta	0·81	0·78	0·71 (0·03)	n.d.	n.d.	2·7 (0·5)	n.d.	1·4 (0·3)	1·12 (0·03)	1·4 (0·2)
Pb	10·3	11·5	11 (1)	51 (11)	57	78 (21)	61 (6)	74 (8)	71·9 (5·23)	42 (3)
Th	6·03	6·1	5·2 (0·2)	1·53 (0·92)	0·86	1·3 (0·4)	1·1 (0·3)	3·5 (1·5)	1·97 (0·19)	13 (2)
U	1·62	1·73	1·5 (0·1)	4·0 (1·2)	2·1	4·5 (1·2)	4·2 (0·4)	2·9 (0·7)	3·62 (0·26)	7·7 (1·1)
La	24·4	24·5	22 (0·6)	2·3 (0·7)	1·7	4·5 (0·9)	4·0 (0·4)	7·5 (3·1)	6·11 (0·19)	20 (4)
Ce	51·9	50·5	47 (2)	6·4 (1·1)	5·1	10 (3)	8·6 (0·5)	17 (7)	17·0 (0·47)	41 (7)
Pr	6·48	6·8	5·8 (0·2)	0·80 (0·16)	0·7	1·1 (0·3)	0·95 (0·08)	2·0 (0·8)	2·21 (0·14)	4·4 (0·8)
Nd	28·4	29	25 (1)	3·3 (0·7)	3·2	4·3 (0·7)	3·4 (0·5)	7·7 (3·2)	9·91 (0·61)	17 (3)
Sm	6·58	6·6	5·7 (0·2)	1·0 (0·3)	0·95	1·3 (0·3)	0·96 (0·18)	1·8 (0·6)	3·48 (0·33)	3·8 (0·5)
Eu	1·98	1·92	1·7 (0·1)	0·26 (0·26)	0·12	1·3 (0·2)	0·78 (0·10)	0·73 (0·28)	0·36 (0·05)	0·97 (0·15)
Gd	6·67	6·5	5·6 (0·2)	1·2 (0·5)	1·4	1·3 (0·3)	1·0 (0·3)	1·8 (0·5)	4·56 (0·43)	3·4 (0·4)
Tb	1·06		0·9 (0·03)	n.d.	n.d.	0·21 (0·06)	n.d.	0·30 (0·06)	0·88 (0·03)	0·5 (0·1)

(continued)

Table 2: Continued

Material:	BCR-2G*	BCR-2G†	BCR-2G‡	MI in Pl	MI in Pl	MI in Grt	MI in Grt	Matrix gl	Matrix gl	Matrix gl
Enclave:	n.a.	n.a.	n.a.	HO-50A	HO-33A	HO-50A	HO-33A	HO-50A	HO-33A	HO-54
No. analyses:	1	1	19–26	18–22	2	2–20	8–12	20–28	2–11	39–48
Dy	6·33	6·5	5·5 (0·2)	1·7 (0·5)	2·5	1·0 (0·4)	0·72 (0·14)	1·9 (0·4)	5·33 (0·27)	3·3 (0·3)
Ho	1·32	1·31	1·1 (0·1)	n.d.	n.d.	0·16 (0·15)	n.d.	0·29 (0·11)	0·77 (0·02)	0·62 (0·05)
Er	3·73	3·6	3·1 (0·1)	0·41 (0·20)	0·51	0·21 (0·10)	0·13 (0·05)	0·67 (0·33)	1·01 (0·23)	1·7 (0·1)
Tm			0·5 (0·02)	n.d.	n.d.	0·05 (0·02)	n.d.	0·09 (0·06)	0·12 (0·02)	0·25 (0·02)
Yb	3·34	3·5	3·0 (0·2)	0·26 (0·18)	0·2	0·09 (0·05)	0·05 (0·03)	0·62 (0·35)	0·46 (0·16)	1·7 (0·1)
Lu	0·5	0·51	0·4 (0·03)	0·05 (0·04)	0·03	0·06 (0·03)	0·02 (0·01)	0·09 (0·06)	0·07 (0·02)	0·24 (0·02)
Zr/Hf	n.a.	n.a.	n.a.	n.d.	n.d.	33·1 (2·90)	n.d.	32·3 (1·1)	34·2 (0·60)	30·5 (1·00)
Nb/Ta	n.a.	n.a.	n.a.	n.d.	n.d.	4·3 (0·4)	n.d.	6·5 (0·5)	7·4 (0·3)	9·8 (0·9)
U/Th	n.a.	n.a.	n.a.	3·4 (1·8)	2·3	3·7 (1·1)	4·1 (1·2)	0·90 (0·32)	1·9 (0·2)	0·61 (0·07)
Th/Ce	n.a.	n.a.	n.a.	0·24 (0·13)	0·17	0·13 (0·04)	0·13 (0·03)	0·20 (0·02)	0·12 (0·01)	0·32 (0·04)
Eu/Eu*	n.a.	n.a.	n.a.	0·69 (0·67)	0·29	3·2 (0·6)	2·5 (0·4)	1·4 (0·7)	0·28 (0·05)	0·84 (0·18)
$(La/Sm)_N$	n.a.	n.a.	n.a.	1·6 (0·6)	1·2	2·5 (0·9)	3·1 (1·0)	2·7 (0·4)	1·2 (0·1)	3·4 (0·2)
$(Gd/Lu)_N$	n.a.	n.a.	n.a.	5·9 (5·2)	6·5	4·0 (2·9)	9·4 (5·7)	3·5 (2·5)	9·0 (4·4)	1·8 (0·2)
$(La/Lu)_N$	n.a.	n.a.	n.a.	11 (11)	6·8	16·2 (16·7)	32·4 (13·0)	13·3 (11·5)	10·5 (5·3)	9·1 (1·8)
Sum REE	n.a.	n.a.	n.a.	18 (3)	16	26 (8)	21 (3)	44 (16)	51 (2)	98 (16)

Material:	Pl	Pl	Pl	Kfs (res)	Kfs (res)	Kfs (new)	Pl (new)	Grt	Grt	Grt
Enclave:	HO-50A	HO-33A	HO-54	HO-50A	HO-33A	HO-50A	HO-33A	HO-50A	HO-33A	HO-54
No. analyses:	18–41	4	8–11	3–5	4–5	5–8	4–5	18–38	28–37	4–6
SiO_2 (wt %)	61·08 (3·24)	56·35 (6·91)	46·20 (4·66)	63·57 (1·10)	62·06 (3·08)	58·82 (5·31)	54·49 (0·78)	39·17 (1·01)	39·40 (1·00)	32·91 (1·13)
Al_2O_3	25·25 (std)	25·25 (std)	30·00 (std)	19·33 (std)	19·33 (std)	19·73 (std)	25·25 (std)	21·72 (std)	21·72 (std)	20·00 (std)
CaO	5·95 (0·33)	5·72 (0·68)	13·02 (0·52)	0·66 (0·06)	0·59 (0·03)	1·25 (0·21)	8·62 (0·63)	0·96 (0·08)	0·88 (0·05)	0·69 (0·04)
P (ppm)	499 (140)	758 (97)	95 (36)	1170 (130)	1290 (90)	n.d.	n.d.	217 (93)	219 (112)	316 (18)
Li	146 (27)	156 (35)	36 (15)	27 (3)	19 (6)	24(4)	95 (12)	19 (3)	19 (4)	20 (1)
Rb	4·2 (3·2)	1·6 (0·3)	3·2 (3·3)	186 (15)	196 (15)	143 (17)	3·1 (0·9)	0·17 (0·22)	0·11 (0·07)	0·10 (0·06)
Cs	0·31 (0·18)	0·03 (0·02)	0·28 (0·26)	1·5 (0·3)	1·1 (0·1)	1·3 (1·2)	0·11 (0·08)	0·04 (0·04)	0·01 (0·01)	0·01 (0·01)
Be	1·1 (0·2)	0·64 (0·20)	1·3 (0·4)	0·07 (0·02)	0·05 (0·02)	0·22 (0·19)	0·38 (0·17)	0·01 (0·01)	0·03 (0·04)	0·02 (0·01)
B	7·5 (4·4)	2·8 (0·4)	8·5 (10·3)	7·5 (4·2)	2·8 (0·9)	7·7 (3·5)	3·8 (2·7)	1·4 (0·9)	1·5 (0·6)	1·1 (0·3)
Sr	1550 (150)	1150 (150)	853 (160)	1300 (50)	924 (23)	2140 (440)	3870 (700)	0·12 (0·19)	0·06 (0·06)	0·14 (0·12)

(continued)

Table 2: Continued

Material:	Pl	Pl	Pl	Kfs (res)	Kfs (res)	Kfs (new)	Pl (new)	Grt	Grt	Grt
Enclave:	HO-50A	HO-33A	HO-54	HO-50A	HO-33A	HO-50A	HO-33A	HO-50A	HO-33A	HO-54
No. analyses:	18–41	4	8–11	3–5	4–5	5–8	4–5	18–38	28–37	4–6
Ba	147 (40)	103 (15)	49 (13)	5290 (420)	4610 (170)	11200 (2750)	2240 (600)	0·32 (0·69)	0·10 (0·19)	0·12 (0·12)
Sc	1·4 (0·2)	1·13 (0·24)	1·15 (0·35)	1·3 (0·2)	1·2 (0·2)	n.d.	n.d.	139 (18)	169 (17)	178 (9)
Ti	62 (31)	34 (5)	102 (42)	76 (20)	68 (16)	222 (35)	36 (15)	58 (29)	77 (28)	43 (13)
V	0·70 (0·84)	0·09 (0·06)	8·0 (2·4)	0·29 (0·25)	0·09 (0·12)	0·27 (0·15)	0·20 (0·24)	43 (22)	47 (23)	39 (4)
Cr	4·0 (2·9)	2·5 (0·5)	7·5 (9·3)	2·0 (0·5)	2·9 (2·1)	n.d.	n.d.	77 (22)	90 (18)	95 (5)
Co	0·65 (1·56)	0·08 (0·06)	1·5 (1·0)	0·10 (0·06)	0·06 (0·03)	n.d.	n.d.	26 (1)	25 (2)	21 (1)
Ni	1·3 (1·6)	0·25 (0·03)	6·8 (5·3)	0·41 (0·25)	0·20 (0·13)	n.d.	n.d.	0·92 (0·59)	0·96 (0·40)	0·95 (0·33)
Cu	8·1 (2·3)	6·0 (0·8)	3·9 (1·3)	2·6 (0·4)	2·1 (0·2)	n.d.	n.d.	0·09 (0·22)	0·09 (0·15)	0·19 (0·16)
Zn	5·1 (3·3)	1·2 (0·3)	7·9 (7·4)	4·1 (1·7)	2·2 (0·3)	12 (7)	3·1 (2·1)	114 (5)	110 (6)	77 (1)
As	0·95 (0·86)	0·12 (0·02)	2·7 (1·7)	0·80 (0·59)	0·17 (0·14)	6·6 (10·0)	0·65 (0·40)	0·15 (0·15)	0·08 (0·04)	0·27 (0·35)
Y	0·61 (0·15)	0·51 (0·23)	0·52 (0·40)	0·36 (0·05)	0·35 (0·01)	1·2 (0·7)	3·2 (1·4)	304 (78)	238 (46)	249 (37)
Zr	0·31 (0·29)	0·06 (0·08)	0·83 (0·68)	0·16 (0·17)	0·04 (0·06)	0·88 (1·71)	0·40 (0·30)	5·6 (2·6)	4·8 (2·1)	6·9 (2·0)
Hf	0·03 (0·04)	0·004	0·06 (0·09)	0·08 (0·02)	0·09 (0·03)	n.d.	n.d.	0·12 (0·05)	0·10 (0·04)	0·15 (0·03)
Nb	0·30 (0·26)	0·01 (0·01)	0·47 (0·83)	0·08 (0·10)	0·02 (0·02)	0·28 (0·53)	0·06 (0·03)	0·23 (0·66)	0·08 (0·13)	0·01 (0·02)
Ta	0·06 (0·05)	0·01 (<0·01)	0·03 (0·03)	0·11 (0·06)	0·18 (0·02)	n.d.	n.d.	0·04 (0·07)	0·04 (0·06)	<0·01 (<0·01)
Pb	105 (15)	93 (12)	4·1 (1·3)	238 (39)	220 (9)	388 (54)	167 (13)	0·04 (0·07)	0·04 (0·06)	0·07 (0·05)
Th	0·02 (0·01)	0·01 (0·01)	0·17 (0·26)	0·02 (0·02)	<0·01 (<0·01)	0·15 (0·21)	0·08 (0·12)	<0·01 (<0·01)	<0·01 (<0·01)	<0·01 (<0·01)
U	0·04 (0·04)	0·01 (<0·01)	0·11 (0·11)	0·06 (0·06)	<0·01 (<0·01)	0·10 (0·13)	0·04 (0·04)	<0·01 (<0·01)	0·01 (0·01)	0·01 (0·01)
La	6·5 (1·5)	6·3 (0·8)	5·2 (2·1)	1·2 (0·1)	0·95 (0·03)	5·6 (1·3)	15 (2)	<0·01 (<0·01)	<0·01 (<0·01)	0·01 (0·01)
Ce	11 (3)	9·9 (1·3)	8·2 (3·5)	1·0 (0·1)	0·75 (0·08)	5·5 (1·5)	26 (4)	0·01 (0·02)	0·01 (0·01)	0·01 (0·01)
Pr	1·0 (0·2)	0·89 (0·10)	0·83 (0·35)	0·05 (0·01)	0·04 (<0·01)	0·34 (0·13)	2·6 (0·5)	<0·01 (<0·01)	<0·01 (<0·01)	0·01 (0·01)
Nd	3·3 (0·8)	2·9 (0·4)	2·9 (1·2)	0·12 (0·06)	0·07 (0·02)	0·75 (0·52)	9·2 (2·2)	0·09 (0·02)	0·08 (0·02)	0·05 (0·02)
Sm	0·59 (0·13)	0·50 (0·08)	0·39 (0·19)	0·03 (0·01)	0·01 (<0·01)	0·20 (0·19)	1·6 (0·6)	0·49 (0·07)	0·34 (0·07)	0·25 (0·09)
Eu	12 (1)	8·8 (1·1)	2·1 (0·5)	12 (0)	8·6 (0·2)	18 (4)	34 (6)	0·10 (0·02)	0·09 (0·02)	0·10 (0·04)
Gd	0·46 (0·10)	0·39 (0·06)	0·22 (0·11)	0·19 (0·07)	0·38 (0·01)	0·32 (0·09)	1·6 (0·5)	4·9 (0·9)	4·2 (1·9)	2·6 (0·8)
Tb	0·05 (0·02)	0·05 (0·01)	0·02 (0·01)	<0·01 (<0·01)	<0·01 (<0·01)	n.d.	n.d.	3·0 (0·5)	2·3 (0·8)	1·6 (0·5)
Dy	0·20 (0·10)	0·20 (0·04)	0·11 (0·08)	0·02 (0·01)	<0·01 (<0·01)	0·10 (0·09)	1·0 (0·4)	41 (7)	31 (7)	27 (6)
Ho	0·02 (0·01)	0·02 (0·01)	0·02 (0·02)	<0·01 (<0·01)	<0·01 (<0·01)	n.d.	n.d.	11 (3)	9·0 (2·6)	9·5 (1·6)
Er	0·03 (0·01)	0·02 (0·01)	0·05 (0·05)	0·01 (<0·01)	0·002	0·14 (0·04)	0·18 (0·09)	32 (11)	31 (14)	34 (9)
Tm	0·01(0·01)	<0·01 (<0·01)	0·01 (0·01)	<0·01 (<0·01)	0·001	n.d.	n.d.	4·5 (1·6)	5·0 (3·0)	5·1 (1·9)

(continued)

Table 2: Continued

Material:	Bt	Bt	Bt	Crd	Crd	Crd	Ilm	Ilm	Ap	Mnz	Zrn	Bulk-rock
Enclave:	HO-50A	HO-33A	HO-54	HO-50A	HO-33A	HO-54	HO-50A	HO-33A	HO-33A	HO-50A	HO-50	HO-50
No. analyses:	9–13	5	8–10	13–20	11–13	1–5	6–10	2	5–6	5–22	1	
SiO_2 (wt %)	33·72 (1·41)	33·98 (0·30)	29·58 (3·82)	52·09 (2·38)	51·11 (1·37)	48·44 (2·06)	0·05 (0·07)	0·09 (0·07)	0·35 (0·37)	0·48 (0·31)	32·45	n.d.
Al_2O_3	19·15 (std)	19·15 (std)	17·00 (2·50)	33·28 (std)	33·28 (std)	33·00 (std)	0·15 (0·04)	0·28 (0·16)	0·18 (0·18)	0·09 (0·11)	n.d.	n.d.
CaO	0·18 (0·12)	0·07 (0·01)	0·12 (0·05)	0·10 (0·01)	0·09 (0·003)	0·11	0·01 (0·01)	0·002 (0·001)	56·00 (std)	0·97 (0·10)	b.d.l.	n.d.
P (ppm)	64 (25)	98 (21)	68 (12)	12 (6)	11 (2)	11 (4)	2·1 (1·1)	3·1 (0·1)	228800 (5200)	168700 (21000)	154	n.d.
Li	62 (21)	69 (34)	30 (7)	172 (27)	171 (19)	70 (8)	9·0 (3·7)	6·5 (1·2)	8·6 (1·7)	0·56 (0·37)	n.d.	74
Rb	447 (24)	467 (13)	349 (49)	6·4 (1·9)	6·0 (0·7)	7·7 (0·2)	0·07 (0·07)	0·01 (0·01)	0·45 (0·37)	1·7 (0·6)	13	128
Cs	17 (3)	13 (0)	12 (3)	2·8 (0·7)	2·8 (0·4)	2·9 (0·2)	0·03 (0·03)	0·02 (0·003)	0·02 (0·02)	0·05 (0·03)	n.d.	5·9
Be	0·44 (0·14)	0·30 (0·06)	0·44 (0·15)	56 (11)	41 (4)	89 (28)	0·01 (0·00)	0·01 (0·01)	0·31 (0·30)	0·11 (0·14)	n.d.	0·7
B	8·6 (3·4)	16 (4)	13 (9)	3·7 (1·4)	2·5 (0·4)	2·3 (1·2)	0·88 (0·32)	0·70 (0·06)	4·2 (2·4)	1·4 (1·2)	n.d.	n.d.
Sr	21 (3)	14 (1)	25 (8)	1·2 (1·3)	0·21 (0·03)	0·79	2·8 (0·6)	2·5 (0·1)	671 (26)	102 (14)	1·8	721
Ba	1310 (60)	1180 (20)	1070 (180)	3·1 (5·1)	0·05 (0·06)	6·4 (6·0)	0·67 (0·57)	0·42 (0·02)	2·5 (1·5)	0·52 (0·60)	n.d.	613
Sc	34 (1)	27 (0)	33 (11)	1·2 (0·1)	0·99 (0·05)	1·4 (0·1)	51·3 (4·4)	38·4 (2·0)	3·7 (2·1)	0·29 (0·20)	n.d.	31
Ti	31600 (8500)	33500 (200)	26300 (4000)	23 (21)	20 (22)	17 (5)	315600 (std)	315600 (std)	3·7 (3·1)	8·0 (5·9)	n.d.	n.d.
V	517 (65)	637 (8)	483 (85)	1·44 (1·33)	0·53 (0·19)	1·94 (2·24)	275 (83)	293 (26)	3·4 (3·5)	0·47 (0·47)	5·5	186
Cr	490 (73)	418 (4)	274 (39)	2·8 (1·5)	2·3 (0·4)	2·5 (1·5)	120 (24)	80 (9·2)	1·6 (0·6)	n.d.	b.d.l.	133
Co	61 (3)	66 (1)	47 (6)	16 (1)	17 (1)	17 (6)	41 (4)	46 (3)	0·8 (0·3)	n.d.	n.d.	19
Ni	125 (7)	149 (2)	102 (22)	11 (1)	13 (1)	20 (13)	24 (6)	31 (1)	2·7 (0·8)	n.d.	n.d.	35
Cu	8·1 (4·1)	4·1 (1·0)	8·4 (5·7)	0·58 (0·34)	0·42 (0·26)	0·56	1·3 (0·5)	1·3 (0·2)	2·8 (2·8)	n.d.	n.d.	19
Zn	498 (17)	512 (6)	292 (113)	194 (11)	192 (6)	95 (30)	326 (35)	341 (21)	30 (25)	0·84 (1·74)	n.d.	152
As	9·0 (14)	0·69 (0·40)	2·0 (1·6)	0·56 (0·72)	0·07 (0·01)	0·12 (0·09)	0·07 (0·02)	0·62 (0·17)	4·4 (1·0)	286 (17)	n.d.	n.d.
Y	0·18 (0·07)	0·25 (0·13)	0·18 (0·08)	0·03 (0·04)	0·02 (0·04)	0·05 (0·03)	0·8 (0·4)	1·0 (0·2)	1690 (360)	13600 (1000)	355	45
Zr	5·0 (0·2)	5·4 (0·3)	5·8 (1·2)	0·09 (0·12)	0·01 (0·01)	0·05 (0·06)	36 (2)	53 (21)	0·80 (0·34)	3·38 (0·95)	464700	n.d.
Hf	0·24 (0·03)	0·26 (0·01)	0·27 (0·05)	0·01 (0·01)	<0·01 (<0·01)	0·01	1·3 (0·1)	1·5 (0·1)	0·02 (0·01)	0·28 (0·16)	8880	n.d.
Nb	81 (2)	82 (1)	63 (9)	0·10 (0·12)	0·02 (0·04)	0·01 (0·01)	627 (12)	655 (5)	0·04 (0·04)	0·25 (0·07)	4·3	21·8
Ta	5·1 (0·2)	4·4 (0)	3·7 (0·6)	0·03 (0·06)	<0·01 (<0·01)	0·004	62 (2)	53 (1)	0·01 (0·01)	0·07 (0·02)	0·9	1·7
Pb	18 (1)	17 (0)	14 (3)	0·45 (0·61)	0·07 (0·01)	0·40 (0·78)	0·32 (0·63)	1·1 (0)	22 (3)	30·8 (2·89)	15	54·6
Th	0·01 (0·01)	0·01 (0·01)	0·04 (0·04)	0·01 (0·01)	<0·01 (<0·01)	0·01 (0·11)	0·02 (0·04)	0·01 (0·01)	2·5 (0·7)	38600 (4300)	103	15·7
U	0·03 (0·02)	0·03 (0·01)	0·11 (0·06)	0·01 (0·02)	<0·01 (<0·01)	0·01 (0·09)	0·08 (0·17)	0·05 (0·01)	32 (7)	6220 (1250)	298	2·53
La	0·06 (0·08)	0·06 (0·09)	0·05 (0·04)	0·02 (0·02)	<0·01 (0·01)	0·25 (0·21)	0·01 (0·01)	0·04 (0·02)	289 (52)	117800 (4300)	0·11	44·7
Ce	0·04 (0·03)	0·01 (0·01)	0·13 (0·12)	0·04 (0·06)	0·01 (0·01)	0·56 (0·38)	0·01 (0·01)	0·01 (<0·01)	953 (173)	222000 (std)	14	89·8
Pr	0·01 (0·02)	0·02 (0·02)	0·01 (0·01)	0·01 (0·01)	<0·01 (<0·01)	0·07 (0·04)	<0·01 (<0·01)	0·01 (<0·01)	151 (27)	262000 (800)	0·14	10·3

(continued)

Table 2: Continued

Material:	Bt	Bt	Bt	Crd	Crd	Crd	Ilm	Ilm	Ap	Mnz	Zrn	Bulk-rock
Enclave:	HO-50A	HO-33A	HO-54	HO-50A	HO-33A	HO-54	HO-50A	HO-33A	HO-33A	HO-50A	HO-50	HO-50
No. analyses:	9–13	5	8–10	13–20	11–13	1–5	6–10	2	5–6	5–22	1	
Nd	0·05 (0·07)	0·06 (0·09)	0·06 (0·05)	0·02 (0·02)	<0·01 (<0·01)	0·26 (0·15)	0·01 (0·01)	0·04 (0·01)	755 (138)	102500 (4000)	2·2	38·1
Sm	0·02 (0·02)	0·01 (0·01)	0·01 (0·01)	0·01 (0·01)	<0·01 (<0·01)	0·06 (0·04)	0·01 (0·01)	0·03 (0·01)	279 (47)	18400 (800)	2·5	7·46
Eu	0·20 (0·02)	0·15 (0·01)	0·18 (0·05)	0·01 (0·01)	<0·01 (<0·01)	0·05 (0·04)	<0·01 (<0·01)	<0·01 (<0·01)	32 (3)	1770 (410)	0·4	6·19
Gd	0·07 (0·07)	0·13 (0·02)	0·10 (0·04)	0·09 (0·01)	<0·01 (<0·01)	0·05 (0·03)	0·03 (0·02)	0·05 (0·02)	422 (55)	14000 (600)	9·8	6·28
Tb	<0·01 (<0·01)	<0·01 (<0·01)	<0·01 (<0·01)	<0·01 (<0·01)	<0·01 (<0·01)	0·01 (0·01)	0·01 (0·01)	0·02 (<0·01)	80 (6)	1520 (230)	2·9	1·08
Dy	0·02 (0·01)	0·02 (0·02)	0·02 (0·02)	0·01 (0·01)	<0·01 (<0·01)	0·03 (0·03)	0·12 (0·05)	0·20 (0·05)	452 (25)	5290 (470)	33	6·77
Ho	<0·01 (<0·01)	<0·01 (<0·01)	<0·01 (<0·01)	<0·01 (<0·01)	<0·01 (<0·01)	0·01 (<0·01)	0·03 (0·02)	0·04 (0·02)	56 (14)	567 (41)	11	1·66
Er	0·01 (0·01)	0·01 (0·01)	0·01 (0·01)	0·01 (<0·01)	<0·01 (<0·01)	0·01 (0·01)	0·11 (0·07)	0·10 (0·03)	86 (45)	882 (102)	55	4·83
Tm	<0·01 (<0·01)	<0·01 (<0·01)	<0·01 (<0·01)	<0·01 (<0·01)	<0·01 (<0·01)	<0·01 (<0·01)	0·03 (0·02)	0·01 (<0·01)	7·3 (4·8)	82 (10)	14	0·78
Yb	0·01 (0·01)	0·02 (0·00)	0·02 (0·01)	0·01 (0·01)	<0·01 (<0·01)	0·02 (0·02)	0·25 (0·21)	0·11 (0·04)	31·3 (20·1)	197 (38)	154	5·08
Lu	<0·01 (<0·01)	<0·01 (<0·01)	<0·01 (<0·01)	<0·01 (<0·01)	<0·01 (<0·01)	<0·01 (<0·01)	0·05 (0·04)	0·02 (0·01)	3·2 (1·7)	11 (2)	29	0·7
Zr/Hf	20·7 (2·70)	21·0 (1·66)	22·4 (3·03)	n.a.	n.a.	n.a.	28·4 (1·55)	35·8 (11·0)	52·0 (12·9)	21·4 (10·0)	52·3	n.a.
Nb/Ta	16·0 (0·57)	18·9 (0·15)	17·4 (1·55)	n.a.	n.a.	n.a.	10·1 (0·34)	12·3 (0·17)	n.a.	n.a.	4·8	12·8
U/Th	n.a.	n.a.	n.a.	n.a.	n.a.	n.a.	n.a.	n.a.	12·9 (1·4)	0·16 (0·04)	2·9	0·16
Th/Ce	n.a.	n.a.	n.a.	n.a.	n.a.	n.a.	n.a.	n.a.	0·003 (0·0004)	0·17 (0·02)	7·4	0·18
Eu/Eu*	18·9 (9·50)	7·3 (1·3)	11·1 (4·0)	2·7 (2·9)	1·3 (1·0)	3·7 (4·4)	0·55 (0·39)	0·10 (0·10)	0·28 (0·03)	0·33 (0·07)	0·24	2·7
$(La/Sm)_N$	4·0 (2·2)	3·5 (2·6)	4·38 (4·72)	1·7 (1·5)	0·61 (0·44)	7·2 (11·1)	0·41 (0·34)	0·90 (0·08)	0·67 (0·02)	4·1 (0·2)	0·03	3·87
$(Gd/Lu)_N$	5·9 (9·8)	6·4 (1·7)	3·5 (2·0)	1·6 (1·6)	1·9 (2·8)	4·1 (4·2)	0·10 (0·08)	0·31 (0·06)	20·0 (8·16)	163 (35)	0·04	1·11
$(La/Lu)_N$	2·8 (2·4)	2·4 (3·5)	1·45 (1·44)	5·8 (11·6)	1·0 (1·8)	25·1 (40·7)	0·02 (0·03)	0·21 (0·15)	12·0 (5·3)	1189 (224)	0·0004	6·88
Sum REE	0·44 (0·18)	0·50 (0·28)	0·54 (0·23)	0·11 (0·12)	0·03 (0·02)	1·4 (0·9)	0·56 (0·32)	0·66 (0·12)	3600 (400)	514400 (17200)	329	224

*Concentrations measured by solution ICP-MS, taken from Norman *et al.* (1998).
†Concentrations measured by LA-ICP-MS, taken from Norman *et al.* (1988).
‡Mean values (and standard deviations) measured in the present study.
'Kfs (res)', residual Kfs; 'Kfs (new)', Kfs crystallized from the melt; 'std', standard (from electron microprobe analysis or stoichiometry) used to normalize and extract trace element concentrations. n.d., not determined. n.a., not applicable; b.d.l., below detection limits. Numbers in parentheses refer to 1σ standard deviations.

Eggins (2003). The precision of single LA-ICP-MS spot analyses was typically 5–10% relative (Kosler, 2001). Silicon, Al, Ca, Ti and Ce contents, determined either by electron microprobe or from the stoichiometric formulae of the mineral phases, were used as internal standards for silicate minerals and glasses (Si: Hbl, Zrn; Al: Bt, Crd, Grt, Pl, Kfs, Spl, glass; Ca: Ap; Ti: Ilm; Ce: Mnz). Data were reduced using an in-house Excel spreadsheet.

Bulk-rock trace-element determinations on HO-50 were carried out by ICP–MS at the Centro de Instrumentación Científica (Universidad de Granada), after HNO_3–HF digestion of 0·1000 g of sample powder in a Teflon-lined vessel at 180°C and 200 p.s.i for 30 min, evaporation to dryness, and subsequent dissolution in 100 ml of 4 vol. % HNO_3. The measurements were carried out in triplicate with a PE SCIEX ELAN-5000 spectrometer using Rh as internal standard. The precision was better than ±5% for an analyte concentration of 10 ppm.

RESULTS

The whole-rock trace element compositions of the enclave HO-50, the silicate glasses and mineral phases of enclaves HO-33 and HO-50 and dacite HO-54, and the secondary standard BCR-2G are presented in Table 2 (mean values and standard deviations) and Figs 3 and 4. Figure 5 shows profiles of the trace element compositions measured across two of the volumetrically most important mineral phases in the enclaves, Pl and Grt.

Trace element composition of glasses

In general and compared with granite analyses, the glasses have very high concentrations of Li, Cs and B, moderate to low concentrations of Rb, Sr, Ba and Be, and low to very low concentrations of the high field strength elements (HFSE) Y, Zr, Hf, U, Th, first row transition elements (FRTE) Sc, V, Cr, Co, Ni, Cu, Zn, and rare earth elements (REE) La to Lu (~0·1–10 × chondrite) (Fig. 4a). Chondrite-normalized REE profiles (using Sun & McDonough, 1989) show flat to slightly negative slopes and variable, moderate negative to positive Eu anomalies (Fig. 4b).

Melt inclusions

Only melt inclusions (hereafter MI) from Pl and Grt were analyzed because those from other minerals were, in general, too small. Melt inclusions in both Pl and Grt show the highest concentrations of typical incompatible elements such as Li (mean Li ~200 ppm), Cs (~30 ppm), Be, B (~200–400 ppm), As and U (~4 ppm). Melt inclusions show also the lowest concentrations of compatible elements such as Sc, Ti, V (~0·5–1·5 ppm) and Cr (and probably all FRTE), and most elements controlled by the dissolution of accessory minerals such as Y, Zr (~25–30 ppm), Th (~1 ppm) and REE ($\sum$REE ~15–25 ppm). The U/Th ratio of MI (~2–5) is the highest of all analyzed glasses, and is much greater than that of the bulk-rock (~0·16), which is dominated by Mnz (U/Th ~0·12–0·20). Conversely, MI show the lowest Nb/Ta ratios (~3–5), much smaller than that of the bulk-rock (Nb/Ta ~13), controlled by Bt (Nb/Ta ~15–19) and Ilm (Nb/Ta ~10–12). We notice, however, that MI have highly variable Li and B, and considerable heterogeneity in Sr, Ba and Ti concentrations and U/Th, Eu/Eu* and La/Lu_N ratios. This is the case for MI hosted by Pl, which appear to contain two separate populations based on the Li concentrations (Table 2, Fig. 3). This compositional variability is observed in MI from both of the analyzed enclave samples (HO-50 and HO-33; Table 2).

Melt inclusions in Pl and Grt show remarkably similar ranges and mean concentrations of those elements incompatible with respect to the mineral hosts such as Li, Rb, Cs, B, Be, Zn, As, Zr, Th, U, Pr, Nd, Sm and Gd (Table 2). Conversely, they show systematic differences in concentrations of the elements Sr, Ba, Eu, La, Ce (compatible or slightly incompatible in Pl, and depleted in MI in Pl), and V, Y and heavy REE (HREE) (compatible in Grt, and depleted in MI in Grt). There are also clear differences in the chondrite-normalized REE patterns. Those of MI in Pl show nearly flat light REE (LREE) (La/Sm_N ~1–2), moderate to low fractionation between LREE and HREE (La/Lu_N ~2–30), and variable though mostly negative to small positive Eu anomalies (Eu/Eu* ~0·2–2). Melt inclusions in Grt show feldspar-like REE patterns, with weak fractionation among the LREE (La/Sm_N ~2–4), moderate to large fractionation between LREE and HREE (La/Lu_N ~10–40) and positive Eu anomalies (Eu/Eu* ~2–4) (Fig. 4b). The Th/Ce ratio of MI in Grt (~0·10–0·16) is comparable with or slightly below that measured on Mnz of enclaves (Th/Ce ~0·15–0·18), which controls the Th/Ce of the bulk-rock (~0·17).

Matrix glasses

Although MI and matrix glasses in enclaves overlap to some extent in composition, they show some differences. Compared with MI, matrix glasses are characterized by lower concentrations of incompatible Li (~100 ppm), Cs (~25 ppm), Be, B (~150–200 ppm), As, but also lower Sr (~30–100 ppm) and U/Th ratios (~0·5–2). Melt inclusions and matrix glasses have comparable concentrations of Rb, Ba, Pb and U, but matrix glasses have higher concentrations of Sc, Ti, V (~1·5–3 ppm), Cr (and probably all FRTE), Y, Zr (~35–65 ppm), Th (~2–3.5 ppm), REE ($\sum$REE ~30–50 ppm) and higher Nb/Ta ratios (~6–7·5).

Matrix glasses show also some compositional variability in Li, U/Th, Eu/Eu* and La/Lu_N. In addition, they show considerable variations in Sr, Ba, Ti, Sc, Y, P, Zr, Th and middle REE (MREE) concentrations, which are far less significant, or have not been observed, in analyses of the MI. Unlike the MI, the compositional variability of

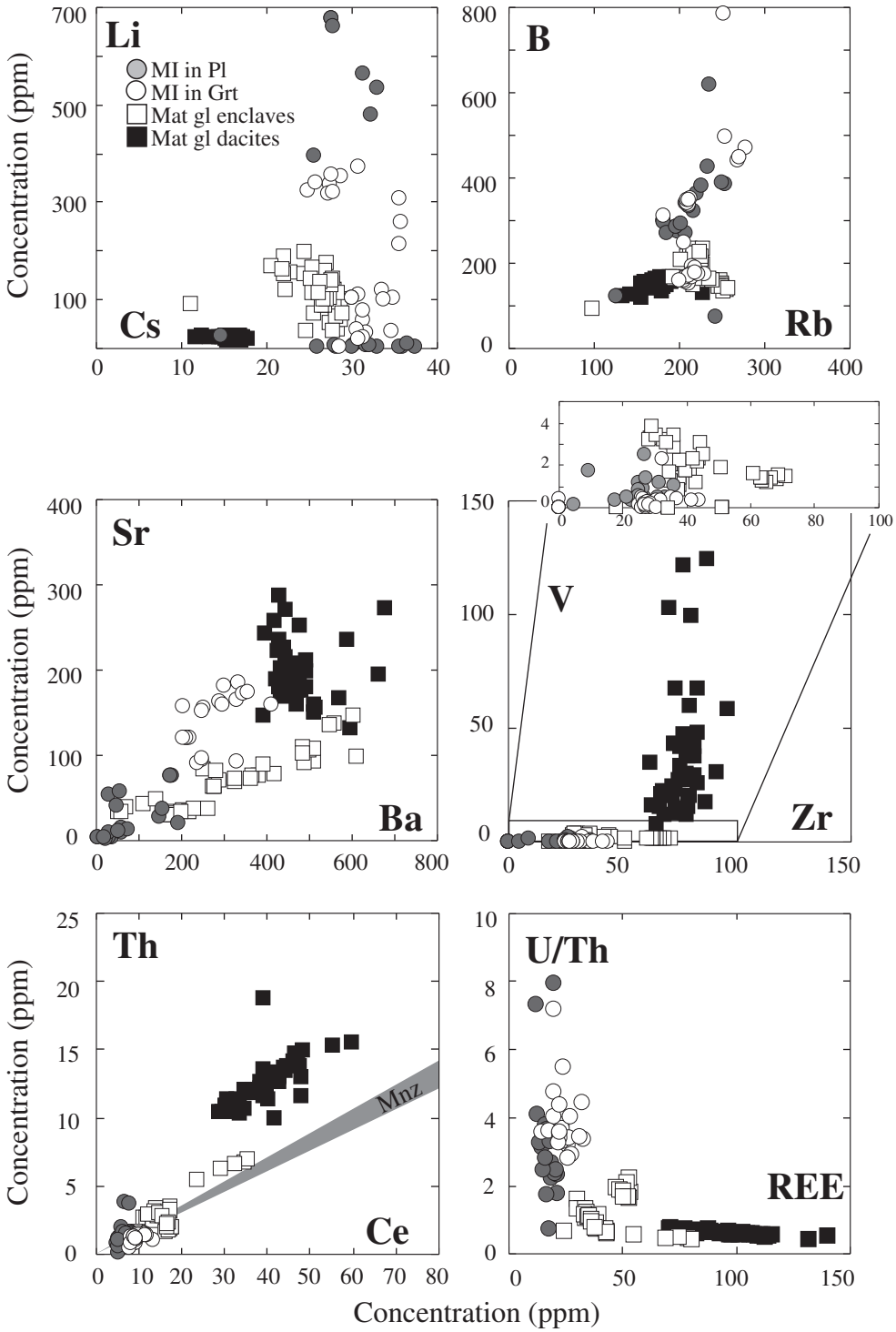

Fig. 3. Variation diagrams showing trace element concentrations and elemental ratios for MI glasses in the Grt–Bt–Sil enclaves and matrix glass in the host El Hoyazo dacite, and the accessory mineral Mnz in the enclaves.

matrix glasses is largely correlated to differences between samples HO-33 and HO-50 (Table 2, Fig. 3). Thus HO-50 has the lowest concentrations of P, Ti, Sc, Y, Zr, MREE and U/Th, and the highest Sr, Eu, Eu/Eu*, Ba, Th and Th/Ce. Chondrite-normalized REE patterns for matrix glasses also differ consistently between the two enclaves. Matrix glasses in HO-50 show somewhat variable patterns, with slight fractionations among the LREE

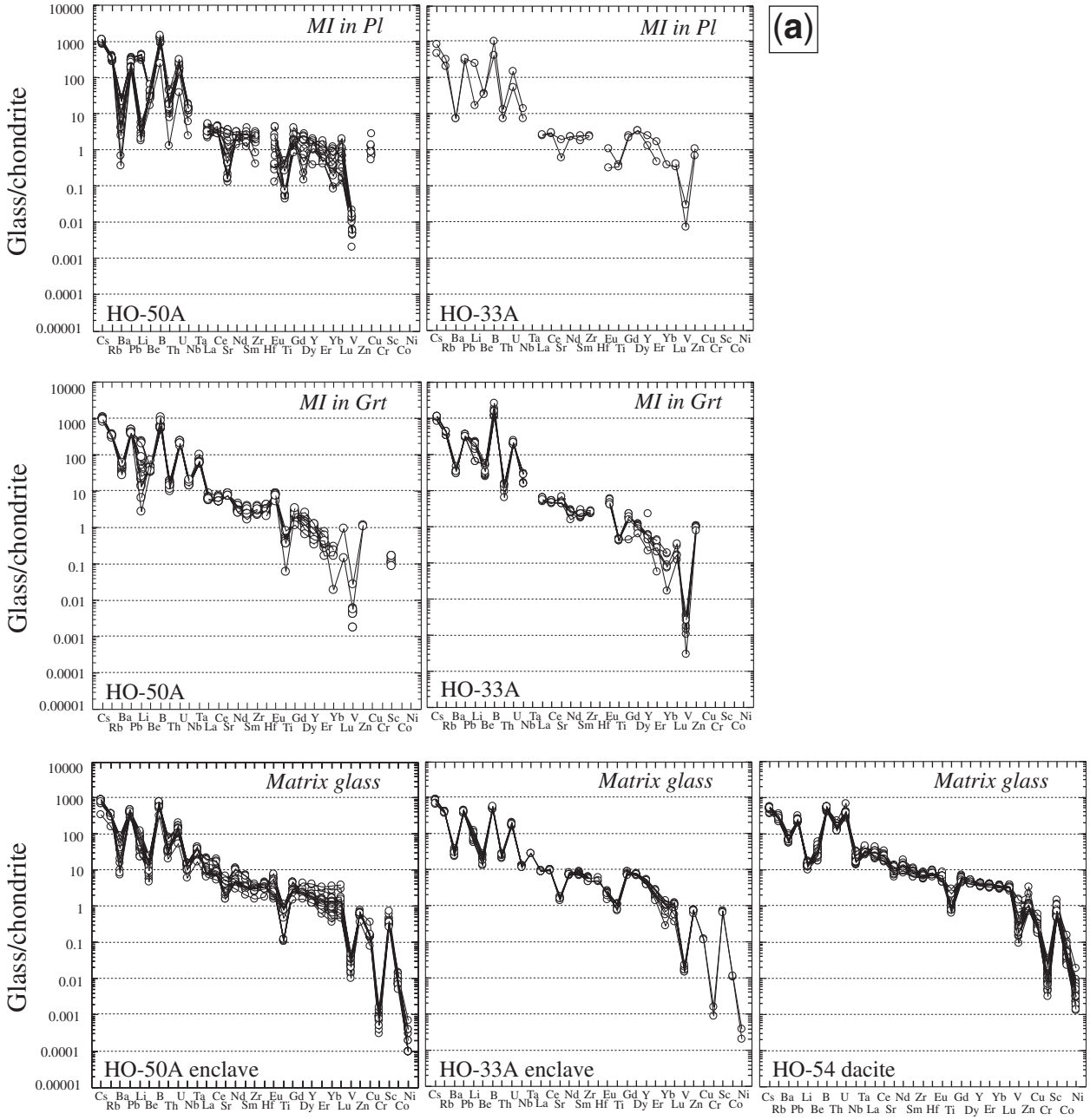

Fig. 4. Chondrite-normalized trace and REE patterns for glasses and minerals of the Grt–Bt–Sil enclaves HO-33 and HO-50 and the host dacite HO-54 (normalizing values from Sun & McDonough, 1989). (a) Normalized trace element patterns for MI and matrix glasses. (b) Chondrite-normalized REE patterns for MI and matrix glasses. (c) Normalized trace element patterns for major mineral phases. (d) Chondrite-normalized REE patterns for major mineral phases. (e) Normalized trace element and REE patterns for accessory mineral phases in the Grt–Bt–Sil enclaves.

(La/Sm_N ~2–3), negative to positive Eu anomalies (Eu/Eu^* ~0·5–2) and moderate to low fractionation among the MREE–HREE (Gd/Lu_N ~1–10) (Fig. 4b). Sample HO-33 has flat LREE profiles (La/Sm_N ~1), moderate negative Eu anomalies (Eu/Eu^*~0·3) and moderate MREE–HREE fractionation (Gd/Lu_N ~6–12). We notice that REE patterns for the matrix glasses of HO-33 resemble those of the analyzed Ap (Fig. 4b and e).

Matrix glasses in dacites show little or no compositional overlap with glasses in the Grt–Bt–Sil enclaves, and have the lowest concentrations of incompatible elements such as Li (~20 ppm), Cs (~16 ppm), Rb and B (~150 ppm); the

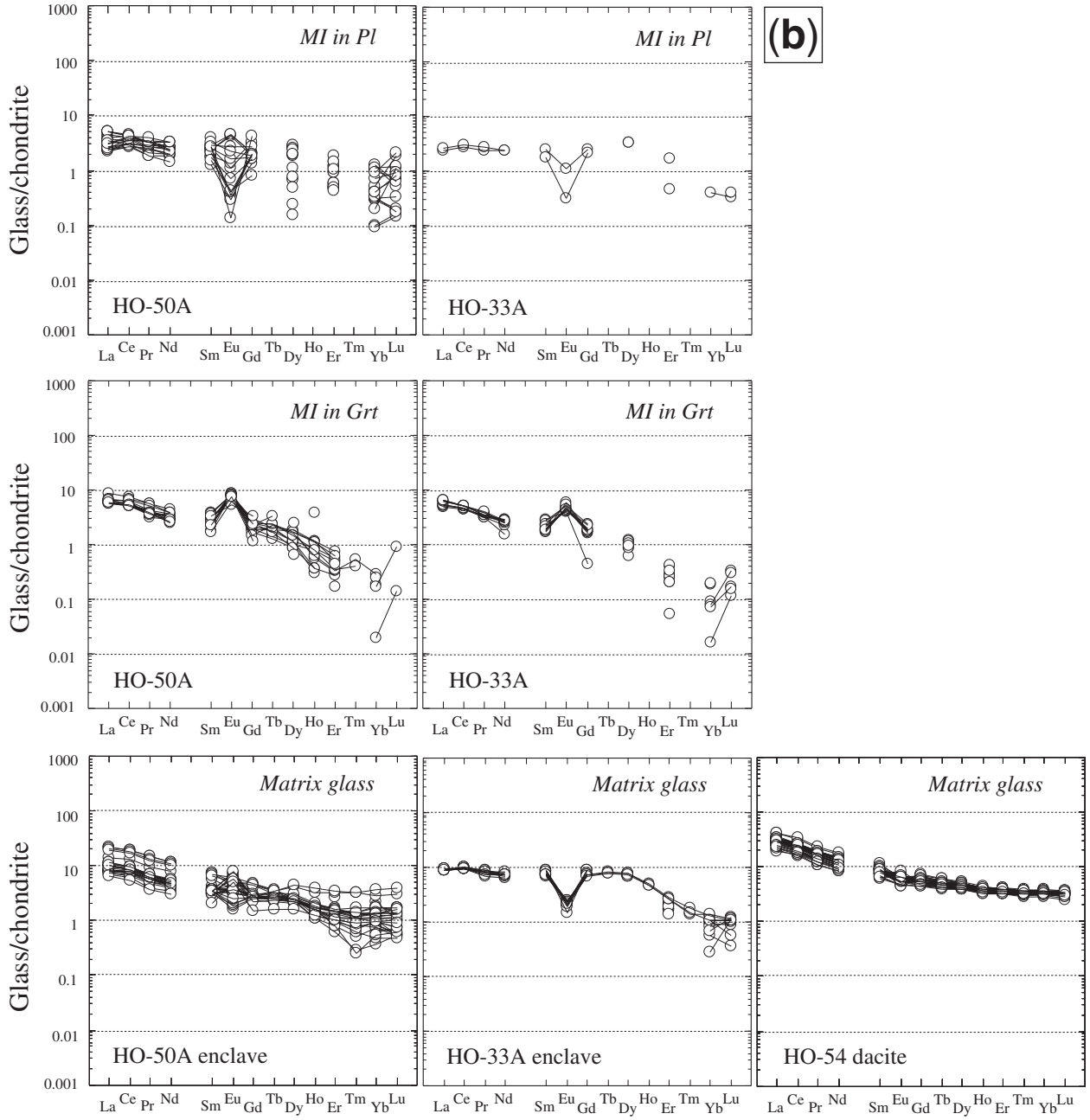

Fig. 4. Continued.

lowest U/Th (~0·4–0·7) ratios; highest concentrations of Sr, Ba (~470 ppm), V (~10–70 ppm), Cr, Co, Ni, Cu, Zr (~65–80 ppm), Th, U (~7–9 ppm) and the REE ($\sum$REE ~75–115 ppm); and the highest Nb/Ta (~9–11) and Th/Ce ratios. The FRTE, and particularly V and Cr, exhibit large variations in concentration (Table 2, Fig. 3). Chondrite-normalized REE patterns are distinct from all other glasses, with moderate fractionation among the LREE (La/Sm_N ~3–4), small negative to negligible Eu anomalies (Eu/Eu* ~0·7–1), and nearly flat MREE–HREE (Gd/Lu_N ~1·5–2).

In summary, MI in Pl and Grt, matrix glasses in the enclaves and dacite matrix glasses plot in separate compositional fields. There is a clear decrease in highly incompatible elements such as Li, Cs and B and a concomitant increase in FRTE, HFSE and REE from the MI to the matrix glass of enclaves to the dacite matrix glasses, such that matrix glasses in the enclaves are roughly

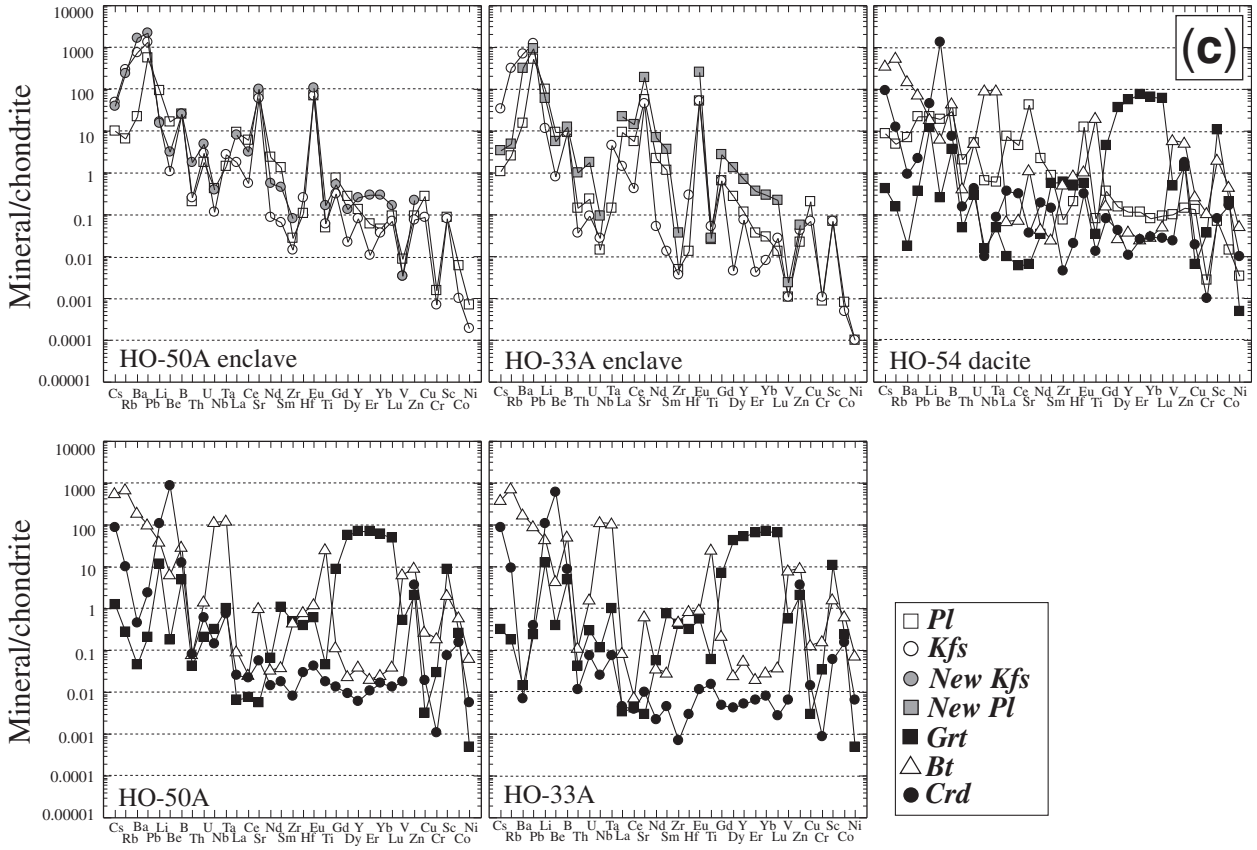

Fig. 4. Continued.

intermediate in composition between MI and matrix glasses in the host dacites. However, the dacite matrix additionally contains significantly higher concentrations of V, Cr and Ni than the glasses in the enclaves.

Trace element composition of mineral phases

Plagioclase

Plagioclase in the enclaves displays the highest concentrations of Sr (comparable with Kfs) and Li (comparable with glass and Crd), and the second highest concentrations of Pb (after Kfs, ~2×). It also shows high concentrations of Eu, P and, to a lesser extent, B, Be, Ba and the LREE (Table 2, Fig. 4c). Chondrite-normalized REE patterns are LREE enriched (La/Lu_N ~100–1000) and show large positive Eu anomalies (Eu/Eu^* ~40–80) (Fig. 4d). Traverses across crystals show clear zoning in major and trace elements, associated with the interface between the MI-rich core and the MI-poor rims (Fig. 5a). At this interface there is a small but apparently sharp decrease in X_{An}, and suddenly a very rapid increase toward the edge; X_{Ab} and X_{Or} show the opposite behavior. Trace elements show either changes in the slope of concentration profiles or compositional breaks at the interface, although patterns are not clear from the currently available profiles. We note, however, that transverses do not show sharp and large increases in X_{An} from core to rim, unlike those found during the experimental melting of Pl in the tonalite or granite systems (Johannes & Holtz, 1992; Acosta-Vigil *et al.*, 2006). Compared with previous trace element analyses of Pl from pelitic migmatites in the granulite facies (e.g. Bea *et al.*, 1994*a*), Pl in the enclaves shows much higher concentrations of Sr (a thousand vs a few hundred ppm) and, surprisingly, Li (a hundred or several tens vs a few ppm). Compared with porphyroblastic, MI-bearing matrix Pl, newly crystallized Pl from matrix glass in the enclaves has higher concentrations of Ba (~10–20×), Sr (~2–4×) and REE (~3×), comparable positive Eu anomalies and Li concentrations (around hundred ppm), and smaller fractionations between the LREE and HREE (La/Lu_N ~100–300) (Fig. 4d). In addition to being much richer in the An component (see above), Pl phenocrysts in the dacite have lower concentrations of P, Li, Pb, Eu, Sr and Ba, higher concentrations of V, Cr and Ni, smaller positive Eu anomalies (Eu/Eu^* ~15–30) and lower relative fractionation between the MREE and HREE (Gd/Lu_N

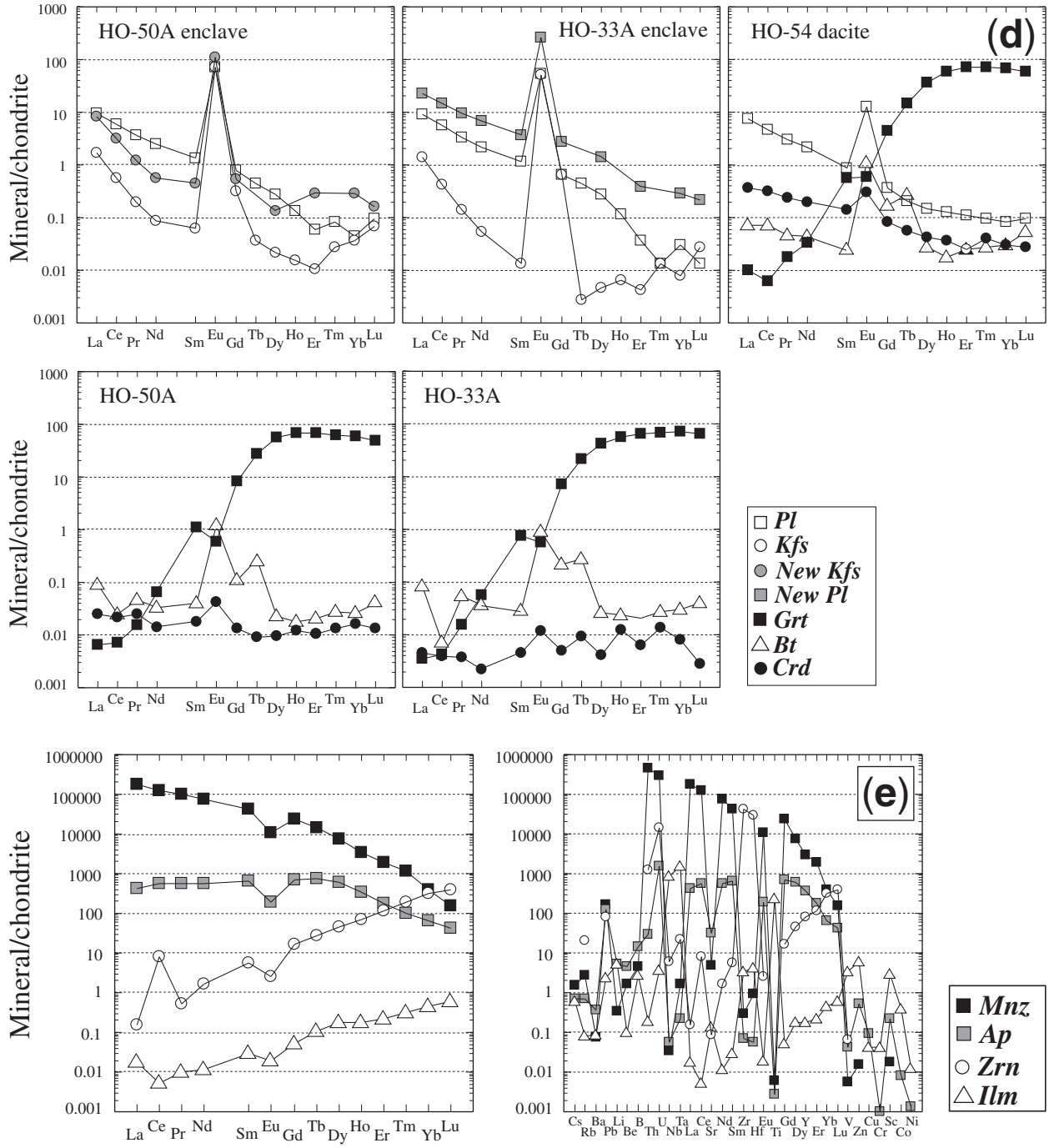

Fig. 4. Continued.

~2–15) with respect to Pl porphyroblasts from the enclaves (Fig. 4d).

Alkali feldspar

Alkali feldspar porphyroblasts have the highest concentrations of Sr (together with Pl), Ba and Pb in the enclaves, and the second highest concentrations of Rb (comparable with glass and after Bt, ~2×). They also concentrate P, Eu and, to a lower degree, Li and B (Table 2, Fig. 4c). Chondrite-normalized REE patterns show larger relative fractionation among the LREE (La/Sm_N ~25–100), larger positive Eu anomalies (Eu/Eu* ~150–550) and

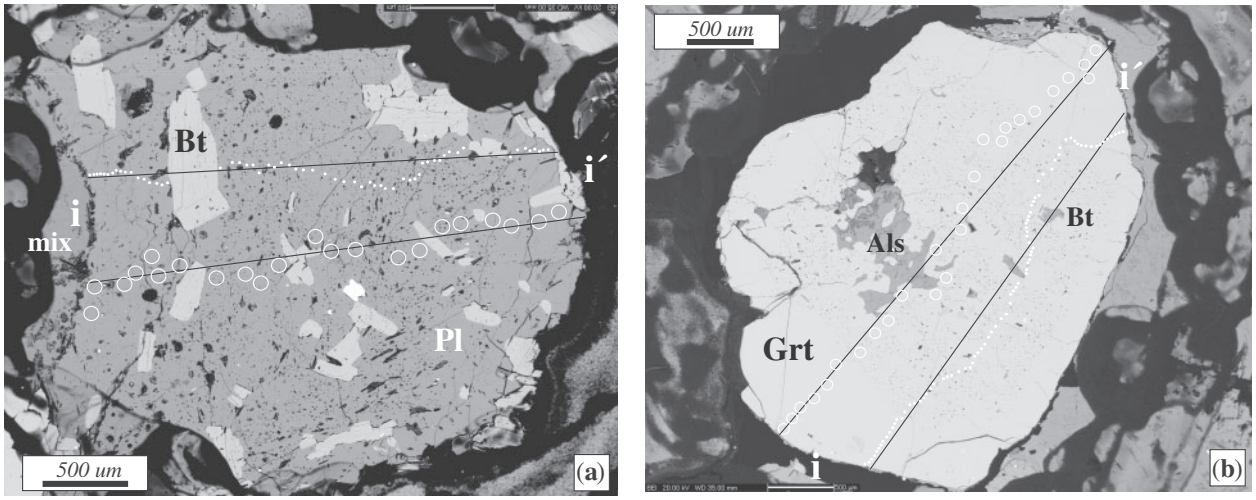

Fig. 5. Backscattered electron images of (a) Pl and (b) Grt crystals, showing the location of LA-ICP-MS (large open circles, scaled to the diameter of the beam ~86 μm) and EMP analyses (small white dots) corresponding to compositional profiles across the crystals. Scale bars represent 500 μm. The results of the analyses of Pl and Grt are shown in (c) and (d), respectively. 'X' refers to molar fraction. #Mg= molar [MgO/(MgO + FeO_t)]. Discontinuous vertical lines show the location of the boundary between MI-rich core and MI-free edge.

lower REE concentrations (~0·3–0·5×) than for Pl porphyroblasts. Compared with Kfs porphyroblasts, newly crystallized Kfs from the matrix glass shows higher concentrations of Sr, Ba, Pb (~2×) and REE (~2–5×), comparable positive Eu anomalies and Li concentrations, and nearly flat MREE and HREE chondrite-normalized REE patterns (Table 2, Fig. 4d). Previous analyses of Kfs in pelitic migmatites from granulite-facies rocks (e.g. Bea *et al.*, 1994*a*; Bea & Montero, 1999) show contrasting MREE and HREE chondrite-normalized profiles and lower Li and, particularly, Sr concentrations than Kfs from the enclaves.

Biotite

Biotite is the most important sink for Rb, V, Cr, Co and Ni in the enclaves, and the second most important reservoir for Cs (after glass, ~2×), Ba (after Kfs, ~3–5×), Sc (comparable with Ilm and after Grt, ~5×), Nb, Ta (Nb/Ta ~15–19) (after Ilm, ~8–10×) and Zn (after trace Spl). It also has relatively high concentrations of Li and, to a lesser extent, Pb and B (Table 2, Fig. 4c). Chondrite-normalized REE abundances are very low (~0·01–0·1× chondrite values, except for Eu ~1× chondrites) and patterns practically flat (La/Lu_N ~0·5–5) except for the positive Eu (Eu/Eu* ~5–15) and negative Ce anomalies of most of the analyses (Fig. 4d). Compared with previously described Bt from pelitic migmatites (e.g. Bea *et al.*, 1994*a*), Bt from the enclaves has higher concentrations of Ba (~3–5×) and Zn (~10×). The trace element composition of biotite phenocrysts from the dacite shows only small differences with respect to that of Bt from enclaves, having lower Li, Zn and Cr concentrations (~0·5×), and no Ce anomaly in chondrite-normalized REE patterns (Fig. 4d).

Garnet

Garnet is the most important reservoir in the enclaves for Sc, and the second most important phase for Cr (after Bt, ~3–4×). It also shows high concentrations of Y and the MREE (Tb to Ho, comparable with Zrn but ~1–3 orders of magnitude lower than in Mnz and Ap), the HREE (Er to Lu, comparable with Ap and ~1 order of magnitude lower than in Mnz) and, to a lesser extent Zn, V, Co and Gd (Fig. 4c). Garnets from the enclaves and xenocrystal Grt in dacites have equivalent trace element compositions (Table 2, Fig. 4c and d). Chondrite-normalized REE patterns show steep positive La to Dy slopes, and slightly positive to flat or even slightly negative Dy to Lu slopes, comparable with garnets described in other granulite-facies pelitic migmatites (e.g. Bea & Montero, 1999). Compared with most of the reported Grt from amphibolite-to-granulite- or granulite-facies migmatites (e.g. Bea *et al.*, 1994*a*; Bea & Montero, 1999; Jung & Hellebrand, 2006; Rubatto *et al.*, 2006), those from the enclaves and dacites show much smaller negative Eu anomalies and contrasting zoning patterns. Garnet porphyroblasts from the enclaves are distinctly zoned in all major and trace elements, and for many elements zoning is truncated around the interface between the MI-rich core and MI-free rim (Fig. 5b).

Cordierite

Cordierite is by far the most important phase concentrating Be in the enclaves. It also shows, together with glass and Pl, the highest concentrations of Li. To a lesser extent, Crd also concentrates Zn, Cs and B (Fig. 4c). Concentrations of REE in Crd (~0·001–0·1× chondrite) are even lower than those in Bt, and chondrite-normalized

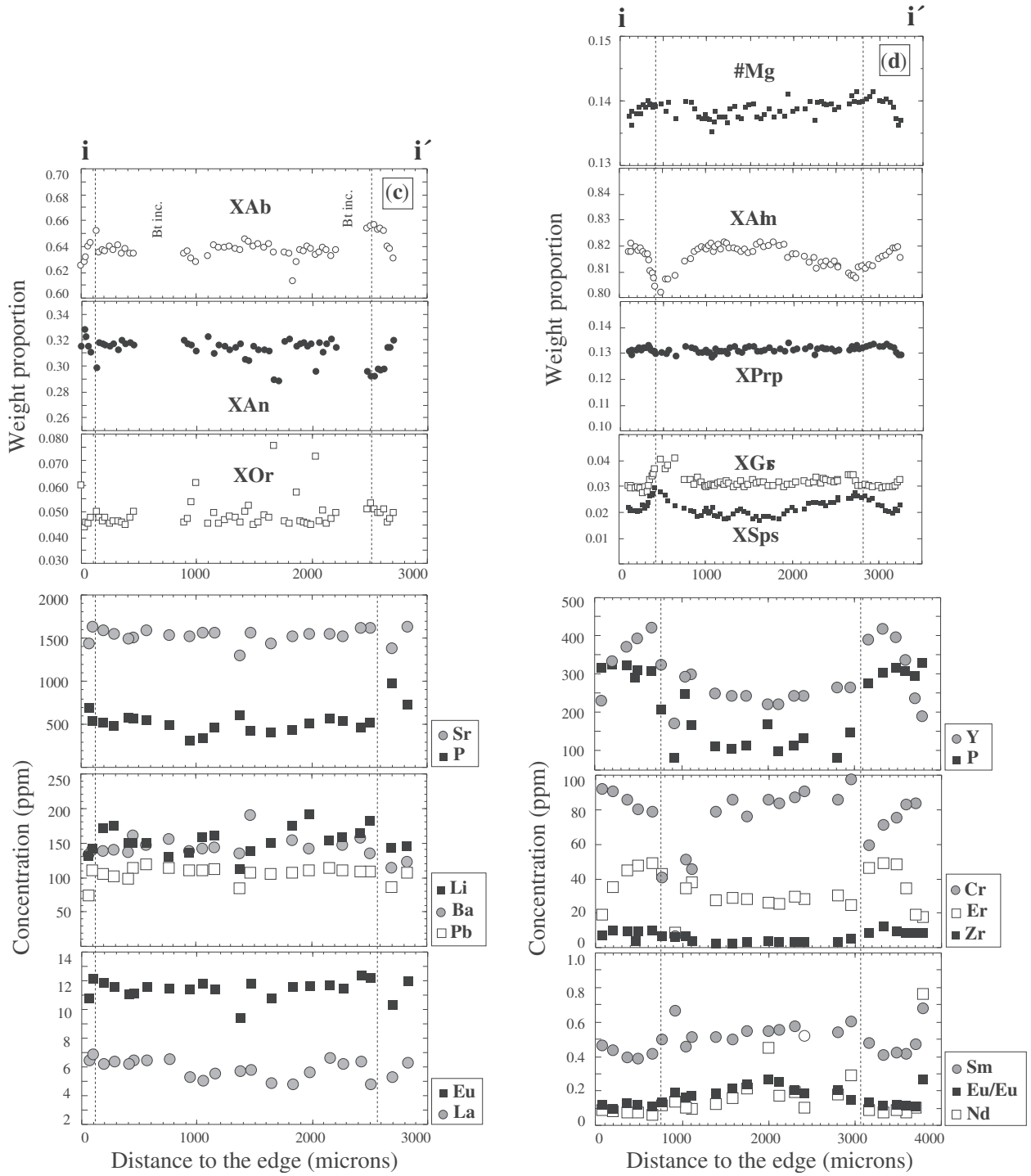

Fig. 5. Continued.

patterns are flat, mostly with small positive Eu anomalies (Eu/Eu* ~1–3) (Fig. 4d). Compared with previously published analyses of Crd in pelitic migmatites (e.g. Bea *et al.*, 1994*a*), Crd in the enclaves has much lower Sr (~0·01–0·1×), Li and Ba (~0·3×) concentrations, much higher Be and Zn (~3–6×) concentrations, and contrasting Eu anomalies (positive vs negative) and chondrite-normalized REE patterns (flat vs 'V'-shaped). Compared with Crd in the enclaves, magmatic Crd phenocrysts in the dacite show higher Be (~2×) and lower Li and Zn (~0·5×)

concentrations, slightly higher REE concentrations ($\sum$REE ~1–2) and fractionation between LREE and HREE (La/Lu_N ~2–10) (Table 2, Fig. 4d). Xenocrystic cordierite in the dacites has similar trace element abundances to that in the enclaves.

Ilmenite

Ilmenite is the mineral phase with the highest concentrations of Nb and Ta (Nb/Ta ~10–12) in the enclaves. It also shows high concentrations of Zn, Sc, V, Cr, Co (similar to those in Bt, 0·5×) and, to a lesser extent Ni, Zr and Hf (Fig. 4c). Rare earth element concentrations are very low and equivalent to those in Bt. Chondrite-normalized REE patterns have gentle positive slopes (La/Lu_N ~0·01–0·3), mostly negative Eu anomalies (Eu/Eu^* ~0·1–1), and positive to negative Ce anomalies (Fig. 4e).

Apatite

Apatite has the second highest concentrations of Y and REE in the enclaves (including Eu, and after Mnz, ~10–200×). It also has high concentrations of Sr, U and, to a lesser extent, Th (U/Th ~11–15), Pb and B (Fig. 4e). Chondrite-normalized REE patterns show slightly positive to flat LREE (La/Sm_N ~0·7), maximum relative abundances for the MREE, moderate negative slopes for MREE and HREE (Gd/Lu_N ~15–25), and moderately negative Eu anomalies (Eu/Eu^* ~0·3). Apatite shows trace element compositions comparable with those of previously analyzed apatites from peraluminous granites and granulitic migmatites (Bea *et al.*, 1994*a*; Bea, 1996*b*), except for lower concentrations of Y and smaller negative Eu anomalies.

Monazite

Monazite shows the highest concentrations by far of U, Th (U/Th ~0·12–0·20), Y and REE (Th/Ce ~0·15–0·18) in the enclaves, and the second highest concentrations of P (after Ap, ~1·5×). It also has high concentrations of As and, to a lesser extent, Sr and Pb. Chondrite-normalized REE patterns show steep negative slopes (La/Lu_N ~1000–1500) and moderate negative Eu anomalies (Eu/Eu^* ~0·3–0·4) (Fig. 4e). These patterns are comparable with those previously described for Mnz from pelitic migmatites (Bea *et al.*, 1994*a*; Bea & Montero, 1999), except for the much smaller negative Eu anomalies (compared with Eu/Eu^* ~0·05–0·002 in previous studies).

Zircon

Besides Zr and Hf (Zr/Hf ~52), zircon from the enclaves shows the highest concentrations of Yb and Lu, the second highest concentrations of Th, U (U/Th ~3, Th/Ce ~7·5) and Tm (well below Mnz), and also considerable contents of Y, Gd to Er (comparable with Grt) and, to a lesser extent, Pb (Table 2, Fig. 4e). The chondrite-normalized REE patterns show positive slopes and large relative fractionation between LREE and HREE (La/Lu_N = 0·0004), a positive Ce anomaly, and a moderate negative Eu anomaly (Eu/Eu^* = 0·24). These features are comparable with those of previously described Zrn from peraluminous granulite-facies migmatites (Rubatto *et al.*, 2006), except for the lower negative Eu anomalies and positive slope of the LREE [vs flat LREE profiles of Bea *et al.* (1994*a*)].

Distribution of trace elements among phases of the Grt–Bt–Sil enclaves

The distribution of trace elements among minerals and glasses in the HO-50 Grt–Bt–Sil enclave has been estimated using the major and trace element bulk composition of the rock, mean major and trace element concentrations for each phase, and a detailed BSE–SEM study on the nature and abundances of accessory minerals in the enclave. The following approach was used. (1) The modal composition of HO-50 was initially estimated by mass balance from the major element composition of the mineral phases, silicate glasses (EMP, Cesare *et al.*, 2005; Acosta-Vigil *et al.*, 2007, and unpublished data) and the bulk-rock [X-ray fluorescence (XRF), Perini *et al.*, 2009]. (2) This modal composition was then used to calculate, together with mean concentrations of trace elements in the various phases (LA-ICP-MS analyses), a model bulk trace element composition for the enclave. (3) Model and measured (XRF, Perini *et al.*, 2009; ICP-MS, Table 2) bulk trace element compositions were then compared to (a) refine the modal abundances of major phases that entirely control certain trace elements (e.g. Pl for Sr, Crd for Be) and, most importantly, (b) estimate the modal abundance of accessory phases such as apatite, zircon and monazite. Final differences between the calculated and measured bulk trace element compositions are ≤15% relative, except for V (~40% rel.), Ni (~25%) and Cu (~73%). Differences in Ni and Cu can be explained by the presence of Py, excluded from the mass-balance calculations. Given the various sources of uncertainty associated with these calculations, these differences are considered reasonable. The calculated modal abundance of phases is reported in Table 1, and the distribution of trace elements among phases of the enclave is shown in Fig. 6. Among the major mineral phases, Pl controls a large proportion (~55–65%) of the Li, Be and Pb, and most (~75–90%) of the Sr and Eu. Biotite hosts ~45–65% of the Cs, Ba, Nb and Ta, and most (~75–95%) of the Rb, V, Cr, Co, Ni and Zn. Garnet controls large amounts (~50–60%) of the Sc and the MREE Dy and Ho, and most (~70–90%) of the Y and HREE (Er to Lu). Despite the low modal abundances, residual Kfs holds ~25% of the Ba, ~10% of the Pb, and ~5% of the Rb, Sr and Eu, whereas ~15% of the Be resides in Crd. Glass (former melt) controls most (~70–80%) of the B and As, and ~45% of the Cs;

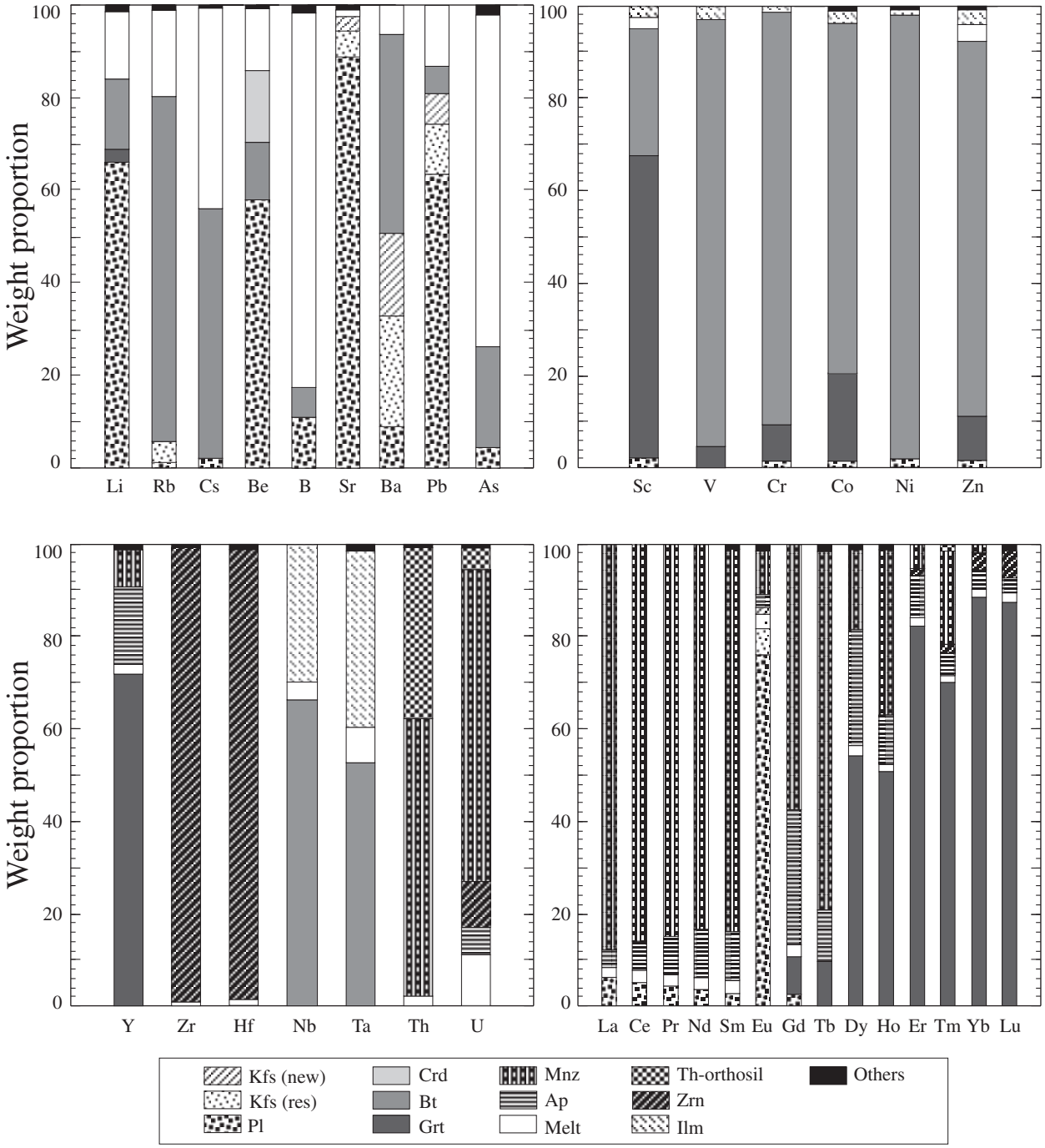

Fig. 6. Distribution of the measured trace elements among phases of the HO-50 Grt–Bt–Sil enclave. (See text for details.) Th-orthosil, Th-orthosilicates; Kfs res, residual alkali feldspar; Kfs new, alkali feldspar crystallized from the melt.

however, it is noteworthy that a large proportion of most of the typically incompatible large ion lithophile elements (LILE) are held in major mineral phases. This provides evidence that significant amounts of these elements can be retained in residual phases up to a relatively high degree of partial melting. Among the accessory phases, Mnz accounts for a large proportion of the Th, U, MREE Gd to Ho, and most (~80–90%) of the La to Sm. Zircon holds ~95% of the Zr, Hf and ~10% of the U. Apatite partially controls (~15–30%) the MREE and Y. About ~35% of the Th and ~5% of the U resides in Th orthosilicates. We notice the absence of xenotime in the enclaves

(if present, it should be in extremely low abundance), and apparently the key role of Grt in the control of Y, the MREE Dy and Ho, and the HREE.

Accessory mineral saturation temperatures

Temperatures for the generation and crystallization of granitic melts (in enclaves and host dacite, respectively) have been calculated from the measured major element, Zr and LREE concentrations in the silicate glasses of the enclaves and the host dacite, and experimental work on the solubility of accessory phases in silicate melts by Watson & Harrison (1984) and Montel (1993). For the Grt–Bt–Sil enclaves, MI in Pl yield the lowest temperatures (~665–715°C) with $T_{Mnz} \sim T_{Zrn}$, whereas MI in Grt (~685–750°C) and matrix glasses (~695–815°C) yield the highest temperatures, with T_{Mnz} equal to or slightly higher than T_{Zrn} (Fig. 7). Results for the two Grt–Bt–Sil enclaves HO-33 and HO-50 are comparable, although small differences exist. Matrix glasses in the host dacites (~750–875°C) show higher saturation temperatures than glasses in the enclaves, always with $T_{Mnz} > T_{Zrn}$. The method applied to analyzing the dacite matrix glass plus microlites using a beam diamenter of 142 μm has the advantage over bulk-rock XRF analyses in that it does not include any inherited zircon and monazite or phenocrysts of these minerals, thus providing a much more accurate estimate of the REE and Zr contents of the dacite melt. It must be noted that, although there is some variation in the temperatures calculated for glasses from each microstructural domain, and T_{Mnz} is generally slightly higher than T_{Zrn}, the accessory mineral saturation temperatures form relatively tight clusters.

Microstructures of accessory minerals in enclaves and host dacite

The meaning of the accessory mineral saturation temperatures, based on Zr and LREE concentrations in melt, depends on the nature, abundance and distribution of accessory minerals in the rock (e.g. Watson *et al.*, 1989; Montel, 1993; Bea, 1996*a*, 1996*b*; see also Brown, 2007). Hence a systematic study on accessory minerals in enclave HO-50 and dacite HO-54 was conducted.

The *in situ* SEM-BSE study of HO-50 shows that, among those accessory minerals important for the budget of trace elements in crustal anatectic rocks, Ap, Zrn and Mnz are by far the most abundant in the enclave. Xenotime has been previously reported in Grt–Bt–Sil enclaves as inclusions in Grt (Muñoz-Espadas *et al.*, 2000); however, it was not observed in HO-50. Most Ap crystals (~75%) appear included in Grt, Bt and, particularly Pl; however, they may contain MI distributed throughout the entire grain (see also Cesare *et al.*, 2003). Apatite inclusions within Pl are anhedral and appear unstable (Fig. 8a),

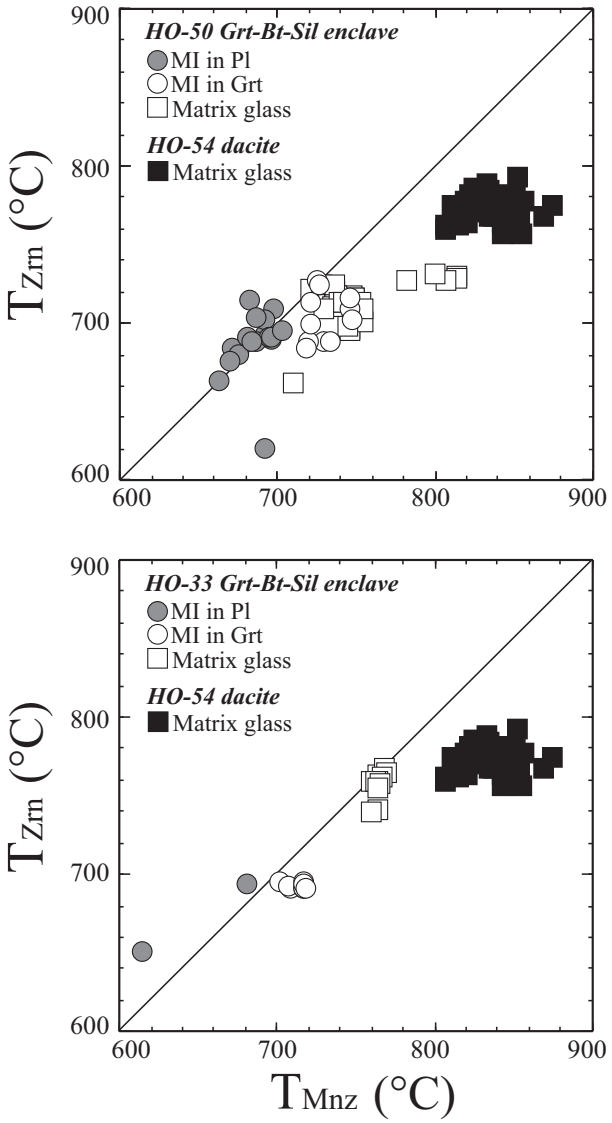

Fig. 7. Zircon and monazite saturation temperatures calculated for all analyzed glasses in enclaves and host dacite. Diagonal line marks the geometrical location of points where both temperatures coincide. (Note the relatively tight groups formed by glasses in each of the microstructural locations.)

suggesting dissolution into the feldspar, whereas Ap included in Grt and Bt or in intergranular locations is euhedral to subhedral and appears stable against the neighbouring phases. Apatite crystals within the Sil–glass 'mix' show euhedral rims apparently grown from the melt (Fig. 8b). A major fraction of the populations of Zrn (~75%) and Mnz (~70%) are also included within the major minerals Pl, Grt, Bt, Crd and Kfs or even other accessory phases such as Ilm. However, most of the Zrn and half of the Mnz grains are subhedral to euhedral and contain small (≤2 μm) melt inclusions, independent of their microstructural location; that is, both inter- and

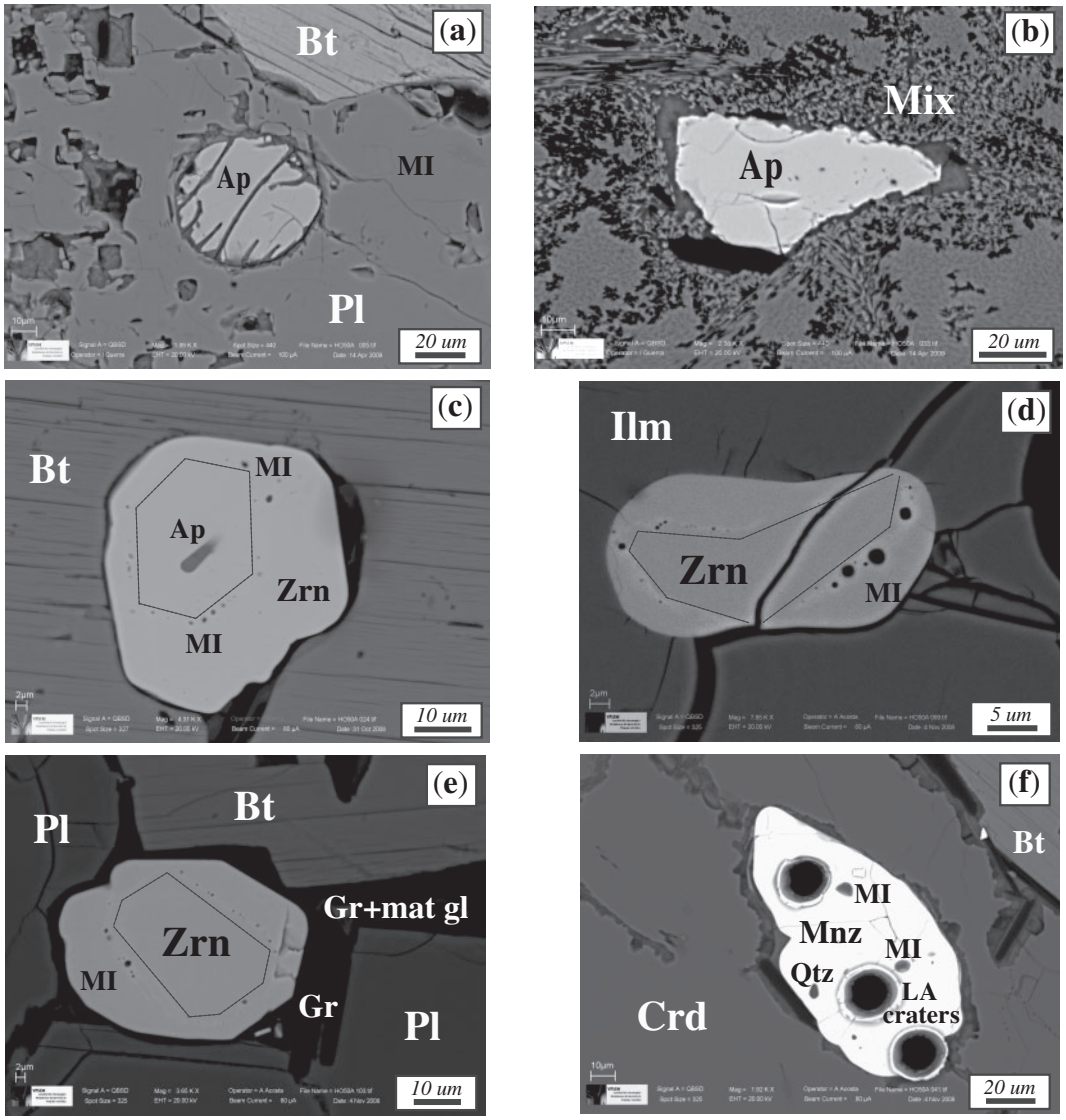

Fig. 8. Backscattered electron (BSE) images of accessory minerals in the HO-50 Grt–Bt–Sil enclave (a–l) and HO-54 dacite (m–p). (a) Anhedral apatite included and apparently dissolving into Pl. (b) Apatite within the Sil + glass intergrowth, showing a subhedral to euhedral rim. (c) Subhedral to euhedral zircon included within Bt. Hereafter the discontinuous line shows the outline of the micron-wide band containing MI and limiting irregular cores and thin subhedral to euhedral rims. (d) Subhedral zircon included in Ilm. (e) Euhedral zircon in the matrix of the enclave, bounded by grains of Bt, Pl and matrix glass. (Note that microstructures of zircons shielded within mineral phases and in the matrix of enclaves in contact with matrix glass are similar.) (f) Subhedral to euhedral monazite included in Crd, showing inclusions of Qtz and glass, and craters produced by LA-ICP-MS analyses using a 19 μm beam. (g) Subhedral to euhedral monazite within the matrix glass, showing inclusions of Bt and MI glass. (Note that the microstructures of monazites shielded within mineral phases and those in the matrix melt are similar.) (h) Zircon and monazite included in Grt. The inset is a close-up view of the included monazite showing that, together with the graphite crystals, this accessory mineral favored the entrapment of MI. (i) Zircon included in Pl. The inset is a close-up view of the included zircon showing that, together with graphite, this accessory mineral favored the entrapment of MI. (Note the two zircon 'branches' growing into the glass pocket and the MI trapped within one of them, giving a perception of mineral growth direction.) (j) Subhedral to euhedral zircon included in Pl and bearing abundant MI distributed throughout most of the zircon grain although showing an asymmetrical distribution. (k) Euhedral and probably entirely (re-)crystallized zircon in the matrix of the enclave and in contact with matrix glass, showing a single and negative crystal shape MI located at the core. (l) Subhedral zircon showing truncation of the internal MI-rich band and external euhedral shape at the contact with the Als + glass intergrowth. (m–o) Dacite showing euhedral Qtz, Pl, Bt, Crd, Opx and Als microlites and accessory minerals Ap, Ilm, Mnz and Zrn in the glassy matrix. Accessory minerals are suhedral to euhedral and vary from a few to tens of micrometers in size; the largest crystals have trapped MI. (See also Fig. 2e and f.) (p) Anhedral monazite in the glassy matrix of the dacite, bearing inclusions of Als and Qtz and possibly representing an inherited and partially dissolved xenocryst from a disaggregated enclave.

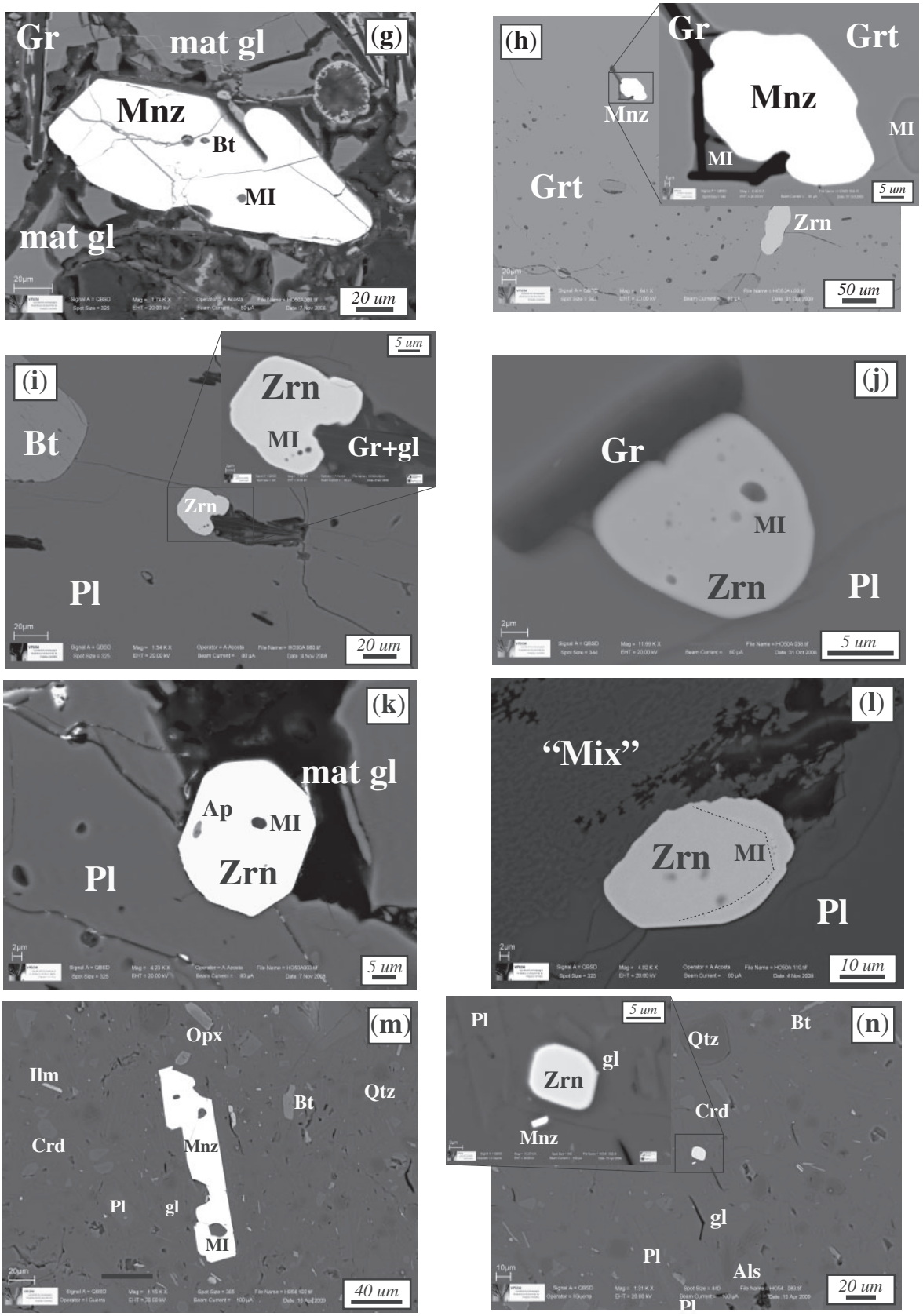

Fig. 8. Continued.

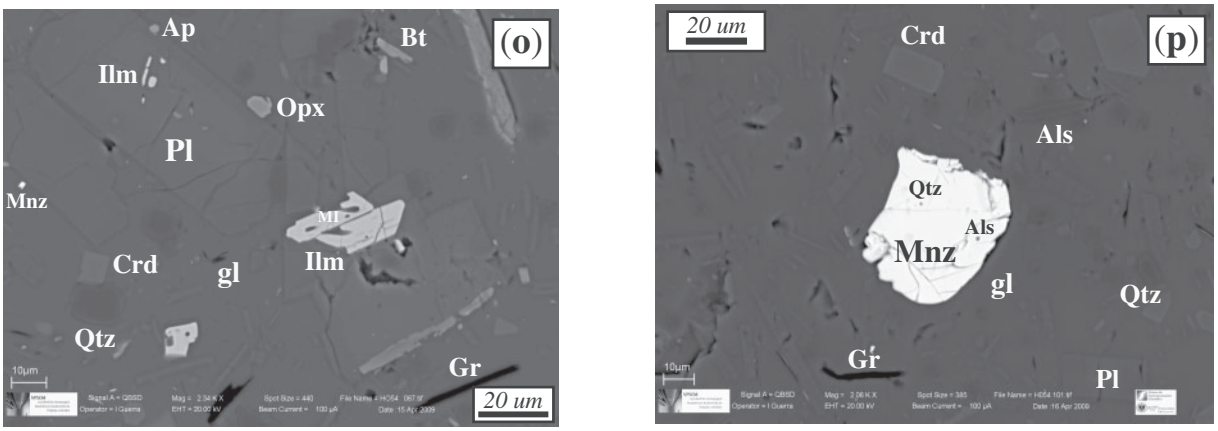

Fig. 8. Continued.

intra-granular grains (Fig. 8c–g). Moreover, microstructures indicate that grains of Zrn and Mnz included in major phases have commonly acted as particles on the surface of the growing minerals that, together with graphite, favored the entrapment of MI (Fig. 8h and i). In most cases where Zrn contains MI, they are distributed within an internal rim separating corroded cores and euhedral rims, as described by Cesare *et al.* (2003, 2009*a*) (Fig. 8c–e). The apparent proportion (surface per cent) of euhedral rims to corroded core ranges from ~10 to 60%, with a mean value of ~35%. In some cases the apparent distribution of MI is very complex or asymmetrical (Fig. 8j). A small fraction of Zrn crystals seem to have entirely (re-)crystallized from the melt phase, as they are small and euhedral with only a few large MI located toward the center (Fig. 8k). Only Zrn grains found within the 'mix' are subhedral to anhedral and locally show truncation of the MI-bearing internal rim (Fig. 8l).

The study of the HO-54 dacite shows that the accessory mineral assemblage of the rock includes Ilm, Ap, Zrn and Mnz, with rare hercynitic spinel, chalcopyrite and chromite. Ilmenite, Zrn, Mnz and Ap appear as euhedral crystals that were probably precipitated from the melt, varying from a few micrometers to tens of micrometers in size; the largest crystals contain MI (Fig. 8m–o). Monazite and Zrn are also present as subhedral to anhedral grains (Fig. 8p) with microstructures that resemble those found in the Grt–Bt–Sil enclaves, and may represent inherited grains as already shown for Zrn by Zeck & Williams (2002).

DISCUSSION

Nature and representativeness of MI composition

Key questions in the study of inclusions are: (1) what phase does the glass in MI represent? (2) How representative is its composition of the bulk composition of that phase in the system (Roedder, 1984)? In addition, it is essential to obtain a large number of high-quality analyses of the glasses to ensure an acceptable estimate and a reasonable interpretation of the composition of these melt inclusions. Careful EMP analyses of a very large (~250) population of MI in Grt–Bt–Sil enclaves, including HO-33 and HO-50, have shown that their major element composition is systematically leucogranitic, peraluminous, and largely comparable with that of glasses (former melts) in metapelite melting experiments (Acosta-Vigil *et al.*, 2007). Hence MI represent a former melt phase (Cesare *et al.*, 1997; Acosta-Vigil *et al.*, 2007), as their glassy nature strongly suggests. Also, Acosta-Vigil *et al.* (2007) recognized that although a combination of post-entrapment processes may have affected to some extent the original compositons, the MI probably represent the composition of the pre-entrapment melt phase in contact with the host, as suggested by their rather common leucogranitic compositions within several mineral hosts. Additional evidence for this conclusion comes from the trace element analyses obtained in this study (see below).

The trapping of melt by (re-)crystallizing mineral phases requires rapid mineral growth ($\sim 10^{-10}$–10^{-8} m/s) to produce destabilization of, and generation of embayments in, the originally planar crystal–melt interface (Baker, 2008, and references therein). The relationships between mineral growth and diffusion rates determine whether compositional boundary layers will form from the melt in front of the growing minerals. Through the experimental generation of MI and numerical modeling of diffusion profiles, Baker (2008) has examined the formation of such boundary layers and the compositions of trapped MI as a function of mineral growth rates, diffusivity of melt species, and diffusive relaxation timescales. His results suggest that for silicic melts and mineral growth rates of $\sim 10^{-8}$–10^{-10} m/s, the measured concentrations of Ba, Be, B, Zr, Nb, U, Th, Y and REE in the MI are the most likely to overestimate to some extent the concentrations of these elements in the bulk melt at the time of entrapment. On the

other hand, concentrations of Cs, Rb, Sr and Li should be close or similar to those of the bulk melt. Nevertheless, the large number (~30–55) of trace element analyses of MI show that, although somewhat heterogeneous, MI in both Pl and Grt have remarkably similar concentrations of those elements that are essentially incompatible with respect to their mineral hosts: Li, Rb, Cs, B, Be, Zn, As, Zr, Pb, Th, U, Pr, Nd, Sm and Gd (Table 2). This points to a melt reservoir with a relatively well-defined geochemical character. The observed concentrations are comparable with those of highly evolved facies of S-type granites (e.g. Bea *et al.*, 1994*b*; Chappell, 1999). Hence we conclude that with respect to the incompatible elements, MI are likely to represent the composition of the pre-entrapment melt in contact with the host crystal, and that this composition is approximately representative of the bulk melt in the system at the time of entrapment.

Interpretation of glass composition: reactions responsible for the production of melt

Although the production of melt in the enclaves may have taken place during rapid recrystallization and melting by a net reaction such as (1), differences in composition between MI and matrix glasses require a detailed analysis of the potential melting reactions in pelitic systems and their role during anatexis at El Hoyazo.

Melt inclusions

Melt inclusions are the remains of the first melts produced during the anatexis of the enclaves that are accessible for study as they are included within the cores of most of the mineral phases. In addition, their compositions probably represent that of the melt phase being produced during the melting reaction and before any extensive interaction with the residue, given the associated high mineral (re-) crystallization rates (e.g. Baker, 2008; see above). Hence, hereafter, we follow the approximation of relating glass geochemistry and potential melt-producing reactions by considering the stoichiometry of typical crustal melting reactions and the trace element compositions of the participant mineral phases, either measured in Grt–Bt–Sil enclaves (Table 2, Fig. 4) or reported in the literature from similar rocks such as high-grade schists and peraluminous migmatites and granites. We also interpret the data in the framework of the model proposed by Cesare & Maineri (1999) on the rapid overstepped melting and (re-)crystallization of a lower-grade metamorphic rock. Besides representing the best known explanation for the presence of MI within both reactants and products of typical melting reactions, this model explains both the extreme abundance of MI, which indicates very rapid (re-)crystallization, and the relative heterogeneity in trace element concentrations in the MI, which is probably due to insufficient time for complete homogenization by diffusion before entrapment.

Major element concentrations in the MI, which probably approach the composition of the bulk-melt during (re-) crystallization of Pl and Grt, strongly suggest partial melting in an H_2O-undersaturated environment (see above; Acosta-Vigil *et al.*, 2007). The trace element analyses of MI in Pl and Grt were conducted on MI from several Pl and Grt grains distributed throughout the entire thin section of samples HO-33 and HO-50. From the above we conclude that, as in the case of the major elements, the concentrations of incompatible trace elements in the MI (including Sr, Eu and LREE of MI in Grt, and V, Y and HREE of MI in Pl) may approach those of the bulk-melt at the time of entrapment (see above and also Frezzotti *et al.*, 2004). Moreover, because concentrations are comparable, it is likely that the entrapment of all MI and recrystallization of Pl and Grt happened at around the same time. In fact, based on microstructural arguments, Pl and Grt have been included within the main equilibrium assemblage of the Grt–Bt–Sil enclaves (Zeck, 1970; Cesare *et al.*, 1997). Because clear differences between MI in Pl and those in Grt are associated with mostly compatible trace elements, we conclude that the concentrations of these elements cannot represent those of the bulk-melt but have been modified by interaction with the host phase, either during or after entrapment. The concentrations of compatible trace elements are considered in more detail in a forthcoming paper on the degree of equilibrium between melts and minerals in the enclaves (Acosta-Vigil *et al.*, in preparation).

Melt inclusions have high concentrations of Li, Cs and B, moderate to low Rb, Sr, Ba and Be, and low to very low Sc, V, Cr, Zn, Y, Zr, Th and REE. The very low concentrations of FRTE Sc, V, Co and Zn, together with moderate to low Rb and Ba, indicate that Bt was stable during the generation of the melt trapped as MI; this limits the formation of MI to temperatures lower than 800–850°C at 5–7 kbar (Vielzeuf & Holloway, 1988; Patiño Douce & Johnston, 1991). The first, lowest temperature, model melting reactions that a pelite (in CNKFMASH) may encounter upon heating at medium pressures are, in order of increasing T (Thompson, 1982; Grant, 1985; Vielzeuf & Holloway, 1988), the H_2O-saturated granite solidus, displaced to lower T by a few tens of °C as a result of the addition of excess Al_2O_3, FeO and MgO:

$$\mathrm{Pl} + \mathrm{Kfs} + \mathrm{Qtz} + \mathrm{Bt} + \mathrm{Ms} + \mathrm{H_2O} = \mathrm{melt} \qquad (2)$$

the H_2O-saturated melting of Ms:

$$\mathrm{Ms} + \mathrm{Bt} + \mathrm{Pl} + \mathrm{Qtz} + \mathrm{H_2O} = \mathrm{Als} + \mathrm{melt} \qquad (3)$$

and the dehydration-melting of Ms:

$$\mathrm{Ms} + \mathrm{Pl} + \mathrm{Qtz} = \mathrm{Bt} + \mathrm{Kfs} + \mathrm{Als} + \mathrm{melt} \qquad (4)$$

Reactions (2) and (3) require a free H_2O-rich fluid initially

present in the lower-grade protolith. Reaction (2) needs, in addition, Kfs as a reactant, and would not be encountered by metapelitic bulk compositions unless pressures were low enough (< ~3·5 kbar) to have allowed sub-solidus breakdown of Ms + Qtz prior to melting; this does not seem to be the case here. Detrital Kfs could be present at low metamorphic grades; however, this would be in the case of more psammitic bulk compositions.

Although we follow the model of rapid overstepped melting of a lower-grade metamorphic rock (Cesare & Maineri, 1999), the protolith may have either partially dehydrated before melting or entered directly the supra-solidus field without producing any free H_2O-rich fluid phase. The following arguments suggest the former possibility as the most likely: (1) the abundance of Bt and Sil in the Grt–Bt–Sil enclaves (see below); and, most importantly, (2) the finding by previous studies that the microstructures of graphite in the enclaves suggest the interation between a C-bearing fluid and a granite melt during generation of the MI (Cesare & Maineri, 1999). Hence melt inclusions should have been generated by one or a combination of reactions (2)–(4).

The experimental study of Buick *et al.* (2004) shows that it is not straightforward to predict what reactions will be kinetically favored and thus active during the rapid heating and melting of a greenschist-facies Chl- and Ms-bearing metapelite. The abundance of Bt and Sil in the Grt–Bt–Sil enclaves indicates that either these phases were already present in the lower-grade protolith and/or they were produced, together with H_2O, during the rapid heating by dehydration reactions involving Ms + Chl ± Grt ± St ± Qtz (e.g. Yardley, 1989). Moreover, Sil + melt (mix) intergrowths in the enclaves strongly suggest the occurrence of a peritectic melting reaction involving Ms, Pl and Qtz (compare with Patiño Douce & Harris, 1998; Buick *et al.*, 2004).

Further constraints on melt-producing reactions are provided by the concentrations of LILE and the Eu anomalies observed in both glasses and minerals. Reactions (2)–(4) indicate that the potential, initially unstable, mineral phases upon heating of the protolith were Ms, Bt, Pl, Qtz and, if present, Kfs. The likely major reservoirs of LILE in the lower-grade protolith of the El Hoyazo enclaves were Chl (Li), Ms (Li, Cs, Ba, Rb, B, Be), Bt (Rb, Ba, Li, Cs, B), Pl (Sr, Li, Be) and, if present, Kfs (Ba, Sr, Rb) (compare with, e.g. Silva & Neiva, 1990; Bea *et al.*, 1994*a*; Harris *et al.*, 1995; Icenhower & London, 1995; Evenson & London, 2003; Bebout *et al.*, 2007). High Li, Cs and B, and moderate to low Rb, Sr, Ba and Be concentrations in the MI suggest, as does the inferred reaction product Sil + glass intergrowths, that Ms and some Pl—together with Qtz to make a granitic composition—were probably the main reactants that formed the early melts that were trapped as MI. The comparatively small negative Eu anomalies in Grt, Zrn and Mnz suggest, on the other hand, that little or no Kfs formed during recrystallization of these phases and entrapment of MI, as these phases show very large negative Eu anomalies in the presence of Kfs (e.g. Bea, 1996*b*; Bea & Montero, 1999; Hermann & Rubatto, 2003; Gregory *et al.*, 2009).

Low concentrations of Y, Zr, Th and REE in the MI indicate limited dissolution of accessory phases such as Ap, Zrn and Mnz during generation of these early melts. This does not seem to be related to a lack of such accessory phases in contact with the melt as ≥50% of the observed Ap, Zrn and Mnz grains in HO-50 contain MI. This observation suggests that, although the majority (~70–75%) of the accessory minerals are currently included within and armored by major mineral phases, a large proportion of them were in contact with the melt phase at the onset of anatexis and to a certain extent dissolved into, and (re-)crystallized from, the melt. Hence the limited dissolution of accessory minerals may be due to either (a) the low T of melting (i.e. the MI were mostly saturated in accessory minerals and T_{Zrn} and T_{Mnz} correspond to the temperature of melt generation), or (b) a short time interval for interaction between accessory phases and the melt (i.e. the MI were undersaturated with respect to the accessories and T_{Zrn} and T_{Mnz} are lower than the temperature of melt generation). Interpretation (a) implies that MI in Pl constitute the earliest record of melts produced in the metapelite, at ~665–715°C, probably by the H_2O-saturated melting of Ms [reaction (3), stage 1 in Fig. 9]. It also implies that Grt (re-)crystallized slightly later than Pl, and that MI in Grt correspond to liquids slightly undersaturated in Zrn (Fig. 7) and probably produced by the dehydration-melting of Ms at ~725–750°C [reaction (4), stage 2 in Fig. 9]. Interpretation (b) implies that most melts trapped as MI were formed at ~725–750°C by the dehydration-melting of Ms (stage 2 in Fig. 9).

It is difficult to evaluate the role of H_2O and hence the dominant melt-forming reactions during the initial stages of anatexis in the enclaves. As suggested by the mineralogy (see above), during rapid heating of the protoliths it is likely that a certain amount of free H_2O-rich fluid was present during the initial stages, immediately after dehydration of phyllosilicates (Chl, Ms) but before the intersection of the wet pelite solidus [see discussion on porosity by Cesare & Maineri (1999)]. In Gr-rich rocks such as the enclaves, GCOH fluids generated by dehydration of the protolith and in equilibrium with Gr have an X_{H2O} ~0·9–0·8 at 700–800°C and 6 kbar (Connolly & Cesare, 1993; Cesare & Maineri, 1999). This fluid would have combined with Ms + Pl + Qtz, as suggested by the geochemical data and accessory mineral saturation temperatures, to produce a certain amount of H_2O-rich granitic melt. For example, the microstructures of graphite in comparable Grt–Bt–Sil enclaves suggest the interaction

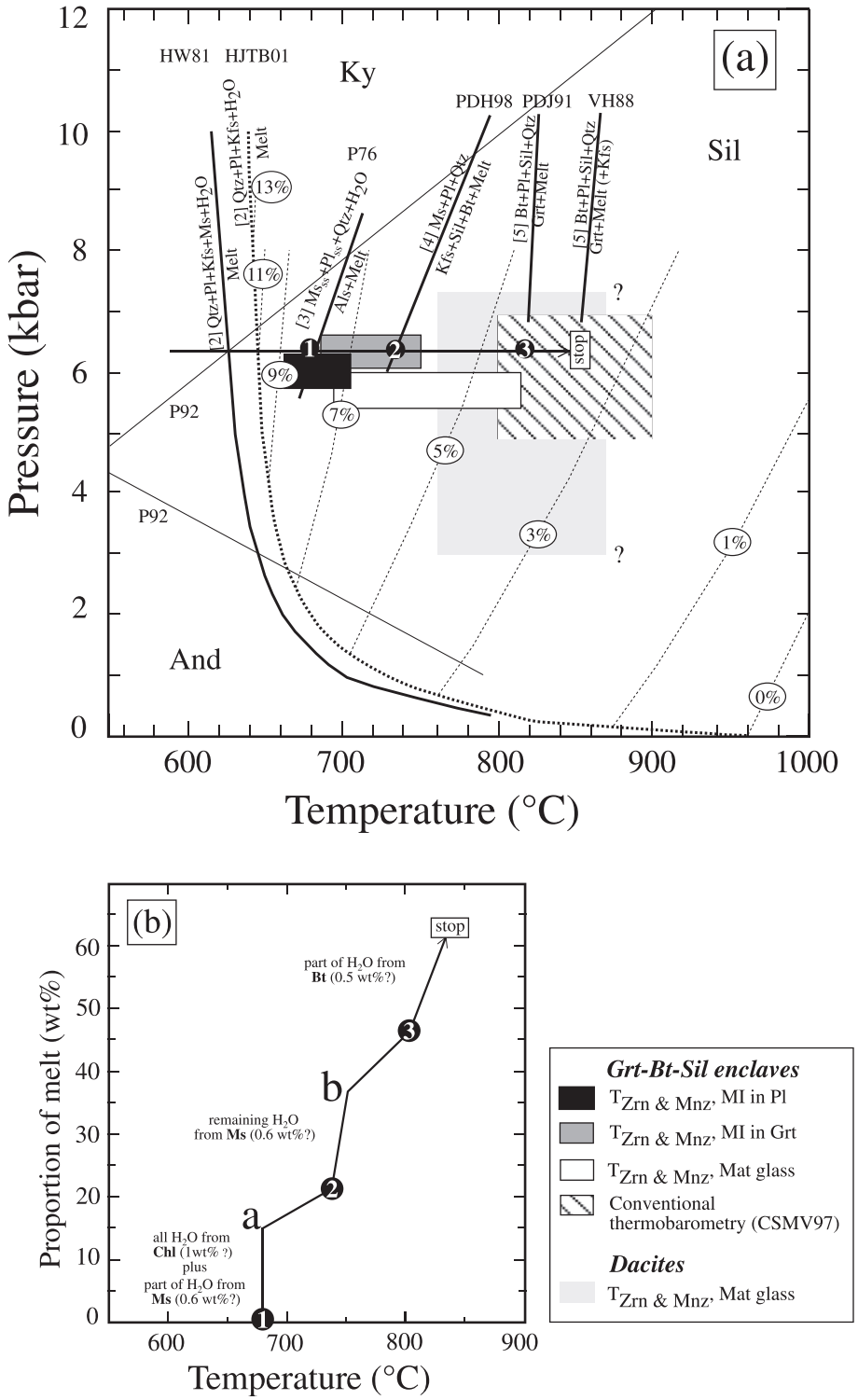

Fig. 9. (a) Pressure and temperature conditions estimated for the enclaves and host dacite, together with relevant experimentally determined melting reactions in the granite and metapelite systems. Pressures of 5–7 kbar have been assigned to accessory mineral saturation temperatures of glasses in the enclaves, after the geobarometric calculations of Cesare *et al.* (1997). Pressures assigned to accessory mineral saturation temperatures of glasses in the dacite matrix are only approximate and take into account the presence of euhedral Grt xenocrysts and Crd phenocrysts. Horizontal arrow refers to the inferred approximate prograde melting path, from the thermobarometric calculations of Cesare *et al.* (1997) and the geochemistry of the glasses. Reactions (2)–(5) refer to those in the text. The wet granite solidus and liquidus curves for the granite

Continued

between granite melt and an H_2O-rich, C-bearing fluid during the generation of the MI (Cesare & Maineri, 1999). The question is whether the quantity of free H_2O-rich fluid was large enough to produce and coexist with a significant proportion of melt at the onset of anatexis.

Assuming that most of the structurally bound H_2O in a greenschist-facies metapelite can be maintained in the system until anatexis commences (e.g. by rapid heating and melting), mass-balance considerations indicate two contrasting scenarios during melting regarding the amount of melt and its a_{H2O}, depending on the reaction pathway and the mineral assemblage present in the rock. On the one hand, a moderate to large amount of H_2O-saturated melt can be produced via reactions (2) and/or (3) if all the H_2O is available (i.e. completely liberated from phyllosilicate) at or close to the wet pelite solidus and can react with the large amounts of Qtz + Kfs + Pl and/or Ms + Pl + Qtz present in the rock (see Buick *et al.*, 2004). On the other hand, a very large proportion of H_2O-undersaturated, low a_{H2O} melt can be generated if a portion of the H_2O remain locked into Ms or Bt until dehydration melting reactions start, and there is enough quartz and feldspars in the system to buffer a_{H2O} at low values [the fluid-absent, rock-dominated system of Clemens & Watkins (2001)]; this scenario maximizes the production of H_2O-undersaturated melt with respect to a situation of slow heating and prograde metamorphism where H_2O from dehydration reactions is lost and the metapelite may start anatexis with water concentrations of only ~1–2 wt %. Thus, considering a concentration of ~3–4 wt % H_2O in the original lower-grade protolith of El Hoyazo enclaves, and that about 1 wt % of this H_2O is still locked into the abundant Bt of the enclaves (Cesare & Maineri, 1999; Table 1), the remaining ~2–3 wt % H_2O may have produced either ~20–25 wt % of an H_2O-rich melt at 700–800°C (a_{H2O} ~0·9–0·8, Connolly & Cesare, 1993) and 5–7 kbar, or ~35–60 wt % of an H_2O-undersaturated melt at 725–800°C (H_2O in the melt ~6–4 wt %; Holtz *et al.*, 2001; Fig. 9b).

Based on the above discussion and the following observations, we conclude that the initially present H_2O-rich fluid dissolved entirely into, and produced a limited amount of H_2O-rich melt; and that although both interpretations (a) and (b), above, are possible, the latter seems more appropriate. (1) Although some of the original H_2O in the glasses in the MI may have been lost after entrapment, the MI are characterized by H_2O concentrations of ~4·5–2·5 wt % (Acosta-Vigil *et al.*, 2007), much lower than values corresponding to a_{H2O} ~0·9–0·8 at 5–7 kbar (~10–9 wt %) and closer to concentrations expected in melts produced by dehydration-melting of Ms (~6 wt %); moreover, several features of the major element geochemistry of the MI strongly suggests melting under H_2O-undersaturated conditions (see above). (2) Major element mass-balance calculations suggest that the extent of melting in the enclaves is around ~30–60 wt % (Cesare *et al.*, 1997), comparable with estimations that assume generation of H_2O-undersaturated melts. (3) Remarkably similar incompatible trace element concentrations in the MI of both Pl and Grt suggest that they represent melts produced by the same melting reaction(s). (4) Melt inclusions in Grt and, particularly, in Pl, show some compositional heterogeneity (e.g. in normative Qtz–Or–Ab, Li, B, U/Th; A. Acosta-Vigil *et al.*, unpublished data; the present paper), suggesting that they represent melts that did not achieve complete equilibrium with the residue before entrapment. Hence, and although T_{Zrn} and T_{Mnz} cluster in the vicinity of potential melting reactions, the melt was possibly slightly undersaturated in the accessory phases Zrn and Mnz. For example, contrasting (~5 vs ~500 ppm) Li concentrations in MI within two adjacent Pl grains (separated by ~7 mm) imply a time interval of tens of days between the generation of the melt and entrapment of the MI, to maintain Li heterogeneities, provided that the melt was interconnected [diffusivities of Li are taken from Henderson *et al.* (1985)]. Along the same line of reasoning and based on mineral growth rates provided by experimental studies to investigate the generation of MI, we estimate that residual and peritectic phases may have (re-)crystallized in a few days to a few years (using growth rates of $\sim 10^{-8}$–10^{-10} m/s, respectively; Baker, 2008

Fig. 9 Continued

eutectic or minimum melt composition at several H_2O concentrations (dotted lines) are taken from Holtz *et al.* (2001). P76 refers to Peto (1976), HW81 to Huang & Wyllie (1981), VH88 to Vielzeuf & Holloway (1988), PDJ91 to Patiño Douce & Johnston (1991); P92 to Pattison (1992), CSMV97 to Cesare *et al.* (1997), PDH98 to Patiño Douce & Harris (1998), and HJTB01 to Holtz *et al.* (2001). (b) Schematic representation of melt production vs temperature along the hypothetical path shown in (a). The path is divided into five segments. Segments starting with 1, 2 and 3 refer to melt produced during reactions (3), (4) and (5), respectively, shown in (a). Segments starting with a and b refer to the increase in melt proportion by dissolution of quartz and feldspars into the melt, as a result of the fixed a_{H2O} in the system at a given P–T and under H_2O-undersaturated conditions in the presence of quartz and feldspars. Calculations have been conducted assuming that the protolith starts anatexis with ~3–4 wt % H_2O distributed between Chl (~1 wt %), Ms (~1·25 wt %) and Bt (~1·25 wt %), and considering that ~0·75 wt % of the initial H_2O remains locked within the abundant Bt (Table 1). (See text for further details.) 'Stop' refers to the highest temperature and melt proportion achieved in the enclaves during the regional melting event.

and references therein). During this time interval Zr may have diffused into the melt away from zircon–melt interfaces for a few to ~150 μm (using the diffusivities of Zr in hydrous granite melts at 700°C, Harrison & Watson, 1983; Mungall *et al.*, 1999); this is a rather short distance for achieving both zircon–melt equilibration and homogenization of Zr in the melt. Nevertheless, considering the previous calculation of diffusion distances and the very low concentrations of Zr in the major mineral phases involved in the melting reaction(s) (~0–5 ppm, Table 2; see also Bea *et al.*, 2006), it is remarkable that the melts actually achieved a uniform Zr concentration of ~20–30 ppm and that T_{Zrn} and T_{Mnz} cluster tightly. This apparently reveals the high capacity of accessory minerals to buffer the concentrations of their essential structural components in the melt at or close to equilibrium values, even in cases of rapid melting and (re-)crystallization such as this.

In summary, microstructural and geochemical data suggest a scenario in which MI formed during the rapid heating and melting of a lower-grade protolith to at least ~700–750°C as indicated by T_{Zrn} and T_{Mnz} (Fig. 9a). Rather than occurring sequentially, melting reactions (3) and (4) probably occurred nearly simultaneously, thus producing a large amount of melt (~30–35 %, Fig. 9b) with H_2O concentrations well below saturation at the pressure of melting, Qtz–Or–Ab normative compositions in the vicinity of low a_{H2O} haplogranite eutectics, and moderate to low ASI values (see Acosta-Vigil *et al.*, 2003). Moreover, such a melting process produces only small amounts of residual K-feldspar (~1–5 wt %, Patiño Douce & Harris, 1998; Pickering & Johnston, 1998), in agreement with our observations (Table 1). The low proportions of this phase may explain the small negative Eu anomalies in Grt and Mnz (see above).

Matrix glasses

The existence of glass as inclusions in all of the minerals and in the rock matrix attests to the presence of melt throughout the entire history of the enclaves as recorded in the observed mineral assemblages. Compositionally, the MI and the matrix glass are sufficiently different to plot in Harker variation diagrams as two populations that only slightly overlap (Fig. 3). From a microstructural point of view, the matrix glasses and MI (particularly those in Pl and Grt) are separated by rims of residual minerals very poor in (in the case of Pl), or free of (in the case of Grt) inclusions of glass (Cesare *et al.*, 1997; Acosta-Vigil *et al.*, 2007). These observations suggest that the generation of the matrix glasses versus the MI probably involved differences in melt-producing reactions and/or perhaps time intervals for the interaction between the melt and the solid assemblage. They also suggest the occurrence of either some time discontinuity in between the generation of MI and matrix glasses, or contrasting associated mineral growth rates.

Compared with the MI, the matrix glasses have lower concentrations of Li, Cs, B, Be, Sr and higher Rb/Cs (~8–10 vs 7–8) and Rb/Li ratios (~2 vs 1); comparable concentrations of Rb, Ba and Pb; and higher FRTE, Y, Zr, Th, REE and Nb/Ta. This shift in the composition of the glasses suggests the destabilization of Bt. The observed mineral assemblage (e.g. virtual absence of Qtz and presence of Crd) and P–T estimations derived from it (800–850°C, 5–7 kbar; Cesare *et al.*, 1997; Tajcmanová *et al.*, 2009), together with the inferred H_2O concentrations (~4·5 wt %), rough positive correlations among Ti, Rb and Zn, and the H_2O-undersaturated Qtz_{36}–Or_{29}–Ab_{35} normative compositions of the matrix glasses (the present study; A. Acosta-Vigil *et al.*, unpublished data), all suggest that the Bt dehydration-melting reaction:

$$Bt + Pl + Sil + Qtz = Grt + Melt\,(+Kfs) \qquad (5)$$

[Grant, 1985; Vielzeuf & Holloway, 1988; reaction (5) and stage 3 in Fig. 9] was involved in the generation of the matrix glasses (see also Cesare *et al.*, 2005). Nevertheless, the still rather high modal abundance of Bt suggests that the matrix glasses are recording only the onset of Bt melting. Thus, the lower concentrations of Li, Cs and Sr in the matrix glasses can be explained by equilibration with abundant Bt and Pl. The lower Be concentrations seem to be related to the appearance of and equilibration with Crd, imposing a Be-depleted geochemical signature to the melt (Evensen & London, 2003). The increase in Ti and FRTE can be associated with the supply of these elements produced by the onset of Bt melting. Higher concentrations of Y, Zr, Th and REE can be related to the higher melting T and potentially the increase in the availability of, or time for the interaction with, accessory phases.

Differences in composition between the matrix glasses of the two analyzed Grt–Bt–Sil enclaves appear to be related to variable contributions of, or degree of equilibrium with, feldspars and accessory phases, and indicate that every single enclave was probably a unique system (e.g. differences in the abundance and distribution of accessory phases, or the late T–t history). Matrix glasses in HO-50 indicate a larger contribution from feldspars (higher Sr, Ba, Eu, Eu/Eu*) and Mnz (higher Th and Th/Ce, lower U/Th). Matrix glasses in HO-33, in contrast, show a greater contribution from Zrn (higher Zr) and Ap (higher U/Th and MREE, lower Th/Ce) relative to Mnz, and less influence of feldspars. It was noted previously that the HO-33 matrix glasses and Ap have very similar chondrite-normalized REE patterns.

The matrix glasses also show some compositional variability within single enclaves, most notably Ti, Li, Sr and Ba (Table 2, Fig. 3) in HO-50. This implies insufficient time for homogenization by diffusion in the melt between

the latest melt-residue reaction (that added material to the melt or subtracted material from it) and quenching upon eruption, provided that the matrix melt was interconneted. This variability can be explained by the progressive reaction history of the enclaves on the way to the surface. Thus, after the regional melting event at $850 \pm 50^{\circ}C$ and 5–7 kbar that produced the glasses and the main mineral assemblage in the enclaves (Cesare *et al.*, 1997; Cesare & Gómez-Pugnaire, 2001), several static and less extensive equilibration stages at lower P are likely to have taken place during the ascent and residence of the magma at shallower crustal levels and before extrusion and quenching. Álvarez-Valero *et al.* (2005, 2007) have inferred an equilibration stage of less than 10^3–10^4 years at shallow depths just before eruption occurred. Heterogeneity in the Ti, Li, Sr and Ba contents of the matrix melt suggests that Pl, Kfs, Bt and Crd were the main mineral phases involved in reactions with the melt during ascent. Indeed, previous studies have described the production of Crd by further reaction of Bt and Pl, and the crystallization of Kfs and Pl from the matrix melt upon quenching (Cesare *et al.*, 2005; Acosta-Vigil *et al.*, 2007). The preservation of variations in the concentration of Ba (~50 vs ~500 ppm) in the matrix glasses of HO-50 over distances of ~12 mm indicates a time interval less than ~100 years between reaction and quenching [using Ba diffusivities in hydrous granite melts at 800°C from Mungall *et al.* (1999)].

Relationships among geochemical, thermobarometric and geochronological data: locating the production of melt along the *P–T–t* path

The compositions of Grt, Bt and Pl hosting abundant MI have been used in thermobarometric calculations to indicate conditions of $850 \pm 50^{\circ}C$ and 5–7 kbar for the main equilibration stage recorded in the Grt–Bt–Sil enclaves (Cesare *et al.*, 1997; Cesare & Gómez-Pugnaire, 2001). These P–T values are well above any Ms melting reaction, and around the dehydration-melting of Bt (Fig. 9). Moreover, the compositions of the MI do not correspond to those of melts generated under such P–T conditions, neither from the point of view of accessory mineral saturation temperatures (Fig. 7), nor from their Li-, Cs- and B-rich, and FRTE-poor signature. In the context of the hypothesis of rapid melting of a greenschist-facies metapelite (Cesare & Maineri, 1999), and considering the previous discussion on the geochemistry and associated T_{Zrn} and T_{Mnz} of the MI, these armoured droplets of melt are interpreted to represent a window into the prograde history of the enclaves, which is otherwise lost by re-equilibration of the phase assemblages and mineral compositions to peak metamorphic conditions. Thus the MI probably record the chemistry of those initial liquids produced during the rapid melting of the pelite at middle to lower crustal pressures, in the T interval ~700–750°C, by Ms melting reactions (see above).

Cesare *et al.* (2003) have shown that Zrn and Mnz concentrates from two Grt–Bt–Sil enclaves (one being HO-33) contain micro-inclusions of glass. They documented that MI in Zrn grains are located within a micrometer-wide band separating irregular cores and thin euhedral to subhedral overgrowths, whereas the MI in Mnz grains are distributed throughout the entire crystal. Recently, Cesare *et al.* (2009*a*) have reported that Zrn and Mnz included in Grt porphyroblasts from HO-50 contain the same distribution of melt inclusions. Zircon overgrowths, interpreted as having crystallized during granulite-facies metamorphism and partial melting, have been dated at $8{\cdot}34 \pm 0{\cdot}45$ Ma [$^{206}Pb/^{238}U$ sensitive high-resolution ion microprobe (SHRIMP) ages, Zeck & Williams, 2002] and $9{\cdot}63 \pm 0{\cdot}26$ Ma ($^{206}Pb/^{238}U$ SHRIMP ages, Cesare *et al.*, 2003). Zircon cores, interpreted as inherited detrital material from the sedimentary protolith, indicate much older ages (late Archean to late Proterozoic, Zeck & Williams, 2002; Cesare *et al.*, 2003). Monazite grains have a $^{238}U/^{206}Pb$ SHRIMP age of $9{\cdot}74 \pm 0{\cdot}21$ Ma, and there is no age difference between cores and rims (Cesare *et al.*, 2003, 2009). The zircon rim ages and the monazite ages should reasonably date the melting event that generated the MI, because: (1) the dated monazite grains contain MI, and the dated rims of zircons are separated from the corroded and older cores by an MI-rich band (Cesare *et al.*, 2003, 2009); (2) a fraction of the dated monazite grains are included, together with MI, within Grt (Cesare *et al.*, 2009); (3) microstructures in Fig. 8 show how zircons included within Pl and Grt, with similar microstructures to the Zrn dated by Cesare *et al.* (2003, 2009), favored the entrapment of, and coexist with, MI. The reader is referred to Cesare *et al.* (2003) for the significance of the zircon rim age differences between Zeck & Williams (2002) and Cesare *et al.* (2003).

The geochemistry of the matrix glasses indicates that a Bt dehydration-melting reaction was probably involved in the generation of the melt present in the matrix of the enclaves (see above). This is in accordance with the comparison between (1) thermobarometric calculations using the composition of minerals from the main assemblage ($850 \pm 50^{\circ}C$, 5–7 kbar; Cesare *et al.*, 1997; Cesare & Gómez-Pugnaire, 2001), whose rims are in contact and mostly in chemical equilibrium with the matrix glasses (Acosta-Vigil *et al.*, in preparation), and (2) experimental studies on the location of the onset of the dehydration-melting of Bt (~800–850°C at 7–10 kbar, Le Breton & Thompson, 1988; Vielzeuf & Holloway, 1988; Patiño Douce & Johnston, 1991). Nevertheless, calculated T_{Zrn} and T_{Mnz} for the matrix glasses (~695–815°C), although higher than those for the MI, show some variability and are at, or below, the minimum temperature

required for Bt dehydration-melting (Fig. 9a). The crystallization of alkali feldspar and plagioclase from the matrix melt necessarily implies some retrogression from the original peak conditions, at least in temperature, if melting took place under H_2O-undersaturated conditions (e.g. Holtz & Johannes, 1994). In fact, most of the accessory mineral saturation temperatures are in the 700–750°C interval. Hence the highest temperatures of ~815°C may be considered as a minimum T for the generation of the matrix melt, in accordance with previous thermobarometric calculations based on mineral chemistry (Fig. 9a).

Zircon and monazite crystals present within the matrix glasses are euhedral and show similar microstructures to those included within the mineral phases (e.g. Grt and Pl, Fig. 8c–g) or those dated by Cesare *et al.* (2003, 2009*a*). Moreover, Cesare *et al.*, 2003) dated zircons and monazites from mineral separates of HO-33, and it is very likely that a fraction of the dated minerals came from the rock matrix, either partially in contact with, or entirely included by, the matrix glass. Hence, with the currently available data, it is reasonable to conclude that both MI and matrix glasses have the same age and therefore represent the continuous production of melt during a single anatectic event at ~9 Ma.

Relationship between the enclaves and the host dacite

Based on petrography, bulk-rock major element and EMP analyses, most of the previous studies at El Hoyazo that have focused on the petrogenesis of the dacite have concluded that the metasedimentary enclaves and the host dacite are genetically related, with the dacite representing to a large extent a magma generated from the anatexis of, and melt extraction from, a crustal protolith similar to the enclaves (Zeck, 1970; Munksgaard, 1984; Cesare *et al.*, 1997, 2009*a*).

The trace element analyses of glasses from Grt–Bt–Sil enclaves and host dacite, reported in this study, however, indicate that the melts present in the Grt–Bt–Sil enclaves and the host dacite are not equivalent in composition. The analyses of glass in the dacite avoided the common micrometer- to millimeter-sized phenocrysts present in the rock, hence they represent the composition of the melt after some crystallization from the original liquid had taken place. Even so, the glassy dacite matrix is lower in incompatible Li and Cs, and higher in compatible Sr, Ba and, particularly, V, Cr, Ni, Zr, Th, U and REE than the MI or glass films within the enclaves. It therefore seems to represent a higher-temperature melt compared with the glasses in the enclaves. Indeed, although the average T_{Mnz} in the dacite matrix glass (~840°C) is in very good agreement with the estimated peak temperature of 850 ± 50°C in the enclaves (Cesare *et al.*, 1997; Cesare & Gómez-Pugnaire, 2001; Fig. 9a), the dacite glasses have accessory mineral saturation temperatures ~50–100°C higher than the matrix glasses in the enclaves (Fig. 7). Moreover, although in many Harker diagrams the glasses from the dacite appear to be roughly collinear with the glasses in the enclaves, suggesting some kind of geochemical progression from MI to enclave glass films to dacite matrix glass, plots involving V, Cr or Ni do not show this trend, but exhibit distinctive fields for each microstructural location (Fig. 3). Similarly, previous studies of the Sr- and Nd-isotope geochemistry of the El Hoyazo rocks point to quasi-equilibrium among the major minerals and glasses in the enclaves, but isotopic disequilibrium both within the host dacite, and between enclaves and dacite (Munksgaard, 1984; Bea, 1996*a*; Perini *et al.*, 2009).

All the above observations necessarily indicate that the connection between the metasedimentary enclaves and the dacite is not as straightforward as the petrographic and bulk major element analyses suggest. Possible reasons for this might be one or a combination of the following. (1) There may be several metasedimentary sources providing material to the dacite magma, one of these being represented by the Grt–Bt–Sil enclaves. In fact, three main mineralogical types of metasedimentary enclaves have been described at El Hoyazo, and previous analyses have shown that at least two of them are isotopically different (the Grt–Bt–Sil and Spl–Crd types, Munksgaard, 1984; Perini *et al.*, 2009). Moreover, a potential source component close in composition to the granite minimum (e.g. a metagreywacke-type) might not be currently represented among the residues, because most or all of it has already entered the melt phase. (2) Lack of chemical equilibrium between the enclaves and the host dacite does not necessarily imply a lack of genetic relationship, as melt–residue disequilibrium seems to be the rule rather than the exception during the process of crustal melting (Bea, 1996*a*). Thus, considering a dacite magma with a minimum equivalent volume corresponding to a sphere of ~1 km in diameter, and a time interval of ~3 Myr between the generation of melt and extrusion (Cesare *et al.*, 2003, 2009*a*), chemical homogenization of the magma by diffusion in the melt is not expected to happen, even for the fastest diffusing components. This can explain the isotopic disequilibrium within the dacite and between the dacite and the metapelitic enclaves. (3) There clearly has been some chemical interaction between the dacite magma and mafic enclaves, as indicated by the occurrence of abundant pyroxene, amphibole and xenocrysts of calcic plagioclase in the dacite, as well as frequent Grt and Qtz xenocrysts or even millimeter-sized fragments of metapelitic enclaves within the the mafic blobs (Zeck, 1992; Fernández-Soler *et al.*, 2007). All of the above indicates that detailed geochemical studies of Spl–Crd and Qtz–Crd metasedimentary enclaves as well as of the mafic enclaves are necessary to

fully understand the relationships between the enclaves and the host dacite and the origin of the dacite.

Models

Based on the above data and discussion we propose an internally consistent model for the mechanism of partial melting of the Grt–Bt–Sil enclaves related to the generation of MI in Pl and Grt. However, the presented data raise some new (and still unresolved) questions regarding the relationships between the enclaves and the host dacite, and hence we present below two alternative interpretations.

A single melting event that relates the enclaves and the dacite

Melt inclusions represent some of the initial silicate liquids formed during the rapid overstepped melting of a lower-grade, H_2O-rich (greenschist-facies?) protolith. Initially, a free H_2O-rich, but C-bearing, fluid was present in the system at the onset of rapid heating, dehydration and nearly contemporaneous melting of the Chl-, Ms- and Gr-rich protolith (see Cesare & Maineri, 1999). Immediately after the enclaves crossed their wet solidus, this H_2O-rich fluid would have dissolved entirely into the limited amount of melt produced (stage 1, Fig. 9). This high a_{H2O} melt, however, has not been recorded by any melt trapped within the minerals. Instead, most of the melting that produced the MI took place under H_2O-undersaturated conditions at temperatures of ~700–750°C, by progressive dissolution of quartz and feldspars into the high a_{H2O} melt with increasing T (stage b, Fig. 9b) and/or by dehydration-melting of Ms (stage 2, Fig. 9). With the existing data it is not entirely clear whether stage 1 and stage 2 of the melting occurred simultaneously or sequentially during rapid heating. Nevertheless, the excess H_2O from Chl- and Ms-dehydration reactions, probably locked within the protolith as a result of the rapid heating and melting, necessarily increased the production of H_2O-undersaturated melt (to about 30–35 wt %, Fig. 9b) compared with a situation of slow heating and prograde metamorphism and melting of a pelite, where dehydration-melting of Ms produces only ~10–15 wt % of melt. Because of the short time interval between melt generation and entrapment (from a few days to a few years), the composition of the MI shows some variation. Nevertheless, the MI have relatively well-defined geochemical characteristics (LILE-rich, FRTE-, HFSE-, REE-poor), which seem to represent the composition of the bulk-melt at this time. After the initial rapid melting and recrystallization there was a decrease in mineral growth rates, indicated by the rims of Pl and Grt with scarce or no MI. This decrease in growth rate was due to the decrease in reaction rates produced by the approach to equilibrium P–T conditions and by the increase in the diameter of the growing crystals. Upon increasing T and between the Ms and Bt dehydration reactions, the proportion of melt increased as a result of the buffering effect of the solid assemblage on a_{H2O} in the melt (stage b, Fig. 9b). The onset of Bt dehydration-melting produced, in addition to an increase in melt proportion, a shift in the composition of the matrix melts toward lower LILE and higher FRTE, HFSE and REE concentrations. Currently available geochronological and microstructural data favor the interpretation that the enclaves crossed their solidus, (re-)crystallized and melted at ~9·6 Ma, producing both MI and matrix glasses, which would represent the continuous production of melt during a single anatectic event (Cesare *et al.*, 2003, 2009*a*). Because eruption of the dacites occurred at ~6·3 Ma (Zeck & Williams, 2002), the enclaves would have been above their solidus and contained melt in contact with the constituent minerals for ~3 Ma (Cesare *et al.*, 2003, 2009*a*). However, reactions taking place upon ascent as a consequence of partial re-equilibration of the enclaves at shallower depths probably produced heterogeneity in the matrix melts in some trace elements such as Ba or the extremely mobile Li, and also the heterogeneous distribution of trace elements within Pl and Grt.

Two melting events and disconnection between enclaves and dacite

The clear differences in composition between the glasses in the enclaves and the matrix glass of the dacite raise some doubts about the genetic relationship proposed above between the metasedimentary enclaves and the host peraluminous dacite at El Hoyazo. This provides an opportunity for new interpretations of the data and suggests the need for further work. As an alternative hypothesis, the enclaves and the host dacite might represent two separate and unrelated crustal melting events. Anatexis in the enclaves took place at ~9·6 Ma, whereas the dacite would have been generated much later and incorporated the enclaves as xenoliths from the deep crust during its final ascent and extrusion at ~6·3 Ma. However, the presence of glass in the enclaves implies either that after partial melting in the middle to lower crust, they cooled down below the solidus very rapidly and the melt did not crystallize but instead solidified mostly as glass; or that the enclaves were remelted during incorporation into the dacite at ~6·3 Ma and the melt quenched upon extrusion. Both possibilities present some problems. Although solidification of a melt to a glass in regional metamorphic migmatites is possible (Cesare *et al.*, 2009*b*), it is highly likely that cooling at pressures of ~5–7 kbar would have largely resulted in the crystallization of the melt (see Holness & Sawyer, 2008; Cesare *et al.*, 2009*b*). Crystallization of the melt would have resulted in exsolution of H_2O, which would have had to have remained sequestered in the system for ~3 Myr to have been involved in the re-melting of the enclaves at ~6·3 Ma. These problems indicate the need to conduct further detailed geochronological and

geochemical studies on the various types of metasedimentary enclave to refine the petrogenesis of the dacite and its relationship with the enclaves.

IMPLICATIONS FOR CRUSTAL ANATEXIS

In addition to providing a precise characterization of the compositions of, and microstructural relationships between, the melt and solid assemblage, this detailed study of quenched anatectic metapelites has the following implications for the study of crustal anatexis.

(1) The high-T melting (~800–850°C) of a metapelite in the middle to lower crust with an initially high proportion of H_2O (~3–4 wt %; e.g. by preservation of most of the structurally bound H_2O contained at greenschist-facies conditions up to the start of anatexis) may result in the production of H_2O-undersaturated melts, such that the extra H_2O does not generate a significant proportion of H_2O-rich melt, but instead maximizes the amount of low a_{H2O} leucogranite melt. Although this situation could be predicted from the point of view of thermodynamics, only the mechanisms and kinetics of the processes determine the final end products. This study shows that the initial excess H_2O can effectively be used to maximize the amount of melt.

(2) Although the temperatures calculated from the concentrations of Zr and LREE in the melt may not always provide very precise constraints on the temperature at which the melt was generated, the dissolution of accessory minerals is significant enough to load the melts with their essential structural components and to provide clues about melting conditions, even in the most adverse situations such as during rapid melting, (re-)crystallization and armouring of both melts and accessories, as shown by the clustering of T_{Zrn} and T_{Mnz} and their closeness to the inferred melting reactions. Thus accessory phases were not melted out and were able to 'buffer' the melt composition in terms of the abundance of trace elements such as Zr, Hf, Th, U and LREE.

(3) The investigated enclaves represent the residues after partial melting at temperatures up to ~850°C and removal of large amounts (~30–60%) of melt (Zeck, 1970; Cesare *et al.*, 1997). The detailed investigation and mass balance of trace elements in the resultant glasses and residual phases (Fig. 6), together with the addition of the extracted melt back into the enclaves, provide evidence that significant amounts of LILE such as Li, Rb, Be, Ba, Pb (~35–45%) and Sr (~90%) can be retained in residual feldspars and biotite up to a high degree of partial melting of the crustal prototith. Also, and in accordance with previous studies (e.g. Bea, 1996*b*), most (~80–95%) of the Zr, Hf, Th and LREE remain locked in accessory minerals such as Zrn, Mnz and, to a lesser extent, Ap and Th-orthosilicates. Hence higher temperatures of partial melting are needed to more efficiently differentiate the crust in these mostly incompatible trace elements. However, we find that a large amount (~80–95%) of the Y and MREE–HREE are controlled by the major phase Grt (see also Reid, 1990), whereas ~50% of the total U seems to have been scavenged by the melt phase.

(4) MI in granulites represent melts that probably record the approximate incompatible trace element concentrations of the bulk melt at the time of entrapment; that is, incompatible elements do not seem to be significantly affected by syn- or post-entrapment modifications.

(5) The composition of melts, if isolated from the system by entrapment within residual or peritectic phases, may represent a window into the pre-peak anatectic history of a migmatite. Hence finding and characterizing former MI in anatectic terranes, although difficult and technically challenging (see Cesare *et al.*, 2009*b*), may provide insights into the anatectic history of the terrane.

(6) In the absence of more detailed studies, the dacite anatectic magma was probably produced by partial melting and the coalescence of melt from several compositionally distinct metasedimentary protoliths; the time span between melt generation and cooling was apparently not long enough for complete homogenization of the melt phase.

ACKNOWLEDGEMENTS

Support for this research was provided by the Australian Research Council (Australian Professorial Fellowship and Discovery Grants No. DP0342473 to I.S.B. and DP0556700 to D.R. and J.H.), the Italian CNR and 01-LECEMA22F WESTMED project by the ESF, the Italian MIUR (grant PRIN 2007278A22), a Ramón y Cajal research contract to A.A.-V., and projects CGL2007-62992, CTM2005-08071-C03-01 and CSD2006-0041 from the Ministerio de Educación y Ciencia of Spain. We are grateful to María Teresa Gómez-Pugnaire, Fernando Gervilla, Juan Manuel Fernández-Soler and Carlos Garrido for discussion and comments, Marjorie Wilson for the editorial work, and Michael Brown, Alberto Patiño-Douce and an anonymous referee for the detailed and encouraging reviews, which improved this contribution.

REFERENCES

Acosta-Vigil, A., London, D., Morgan, G. B., VI, & Dewers, T. A. (2003). Solubility of excess alumina in hydrous granitic melts in

equilibrium with peraluminous minerals at 700–800°C and 200 MPa, and applications of the aluminum saturation index. *Contributions to Mineralogy and Petrology* **146**, 100–119.

Acosta-Vigil, A., London, D. & Morgan, G. B., VI (2006). Experiments on the kinetics of partial melting of a leucogranite at 200 MPa H_2O and 690–800°C: compositional variability of melts during the onset of H_2O-saturated crustal anatexis. *Contributions to Mineralogy and Petrology* **151**, 539–557.

Acosta-Vigil, A., Cesare, B., London, D. & Morgan, G. B., VI (2007). Microstructures and composition of melt inclusions in a crustal anatectic environment, represented by metapelitic enclaves within El Hoyazo dacites, SE Spain. *Chemical Geology* **235**, 450–465.

Álvarez-Valero, A., Cesare, B. & Kriegsman, L. M. (2005). Formation of elliptical garnet in a metapelitic enclave by melt-assisted dissolution and reprecipitation. *Journal of Metamorphic Geology* **23**, 65–74.

Álvarez-Valero, A., Cesare, B. & Kriegsman, L. M. (2007). Formation of spinel–cordierite–feldspar–glass coronas after garnet in metapelitic xenoliths: reaction modeling and geodynamic implications. *Journal of Metamorphic Geology* **25**, 305–320.

Baker, D. R. (2008). The fidelity of melt inclusions as records of melt composition. *Contributions to Mineralogy and Petrology* **156**, 377–395.

Bea, F. (1996*a*). Controls on the trace element composition of crustal melts. *Transactions of the Royal Society of Edinburgh: Earth Sciences* **87**, 33–41.

Bea, F. (1996*b*). Residence of REE, Y, Th and U in granites and crustal protoliths; implications for the chemistry of crustal melts. *Journal of Petrology* **37**, 521–552.

Bea, F. & Montero, P. (1999). Behavior of accessory phases and redistribution of Zr, REE, Y, Th, and U during metamorphism and partial melting of metapelites in the lower crust: an example from the Kinzigite Formation of Ivrea–Verbano, NW Italy. *Geochimica et Cosmochimica Acta* **63**, 1133–1153.

Bea, F., Pereira, M.D. & Stroh, A. (1994*a*). Mineral/leucosome trace-element partitioning in a peraluminous migmatite (a laser ablation-ICP-MS study). *Chemical Geology* **117**, 291–312.

Bea, F., Pereira, M. D., Corretgé, L. G. & Fershtater, G. B. (1994*b*). Differentiation of strongly peraluminous, perphosphorus granites: the Pedrobernardo pluton, central Spain. *Geochimica et Cosmochimica Acta* **58**, 2609–2628.

Bea, F., Montero, P. & Ortega, M. (2006). A LA-ICP-MS evaluation of Zr reservoirs in common crustal rocks: implications for Zr and Hf geochemistry, and zircon-forming processes. *Canadian Mineralogist* **44**, 693–714.

Bebout, G. E., Bebout, A. E. & Graham, C. M. (2007). Cycling of B, Li and LILE (K, Cs, Rb, Ba, Sr) into subduction zones: SIMS evidence from micas in high-P/T metasedimentary rocks. *Chemical Geology* **239**, 284–304.

Benito, R., López-Ruiz, J., Cebriá, J. M., Hertogen, J., Doblas, M., Oyarzun, R. & Demaiffe, D. (1999). Sr and O isotope constraints on source and crustal contamination in the high-K calc-alkaline and shoshonitic Neogene volcanic rocks of SE Spain. *Lithos* **46**, 773–802.

Brown, M. (2002). Retrograde processes in migmatites and granulites revisited. *Journal of Metamorphic Geology* **20**, 25–40.

Brown, M. (2007). Crustal melting and melt extraction, ascent and emplacement in orogens: mechanisms and consequences. *Journal of the Geological Society, London* **164**, 709–730.

Brown, M., Averkin, Y. A., McLellan, E. L. & Sawyer, E. W. (1995). Melt segregation in migmatites. *Journal of Geophysical Research* **100**, 15655–15697.

Buick, I. S., Stevens, G. & Gibson, R. L. (2004). The role of water retention in the anatexis of metapelites in the Bushveld Complex Aureole, South Africa: an experimental study. *Journal of Petrology* **45**, 1777–1797.

Cesare, B. (2000). Incongruent melting of biotite to spinel in a quartz-free restite at El Joyazo (SE Spain): textures and reaction characterization. *Contributions to Mineralogy and Petrology* **139**, 273–284.

Cesare, B. (2008). Crustal melting: working with enclaves. In: Sawyer, E. W. & Brown, M. (eds) *Working with Migmatites. Mineralogical Association of Canada, Short Course* **38**, 37–55.

Cesare, B. & Gómez-Pugnaire, M. T. (2001). Crustal melting in the Alborán domain: constraints from enclaves of the Neogene Volcanic Province. *Physics and Chemistry of the Earth* **26**, 255–260.

Cesare, B. & Maineri, C. (1999). Fluid-present anatexis of metapelites at El Joyazo (SE Spain): constraints from Raman spectroscopy of graphite. *Contributions to Mineralogy and Petrology* **135**, 41–52.

Cesare, B., Salvioli Mariani, E. & Venturelli, G. (1997). Crustal anatexis and melt extraction during deformation in the restitic xenoliths at El Joyazo (SE Spain). *Mineralogical Magazine* **61**, 15–27.

Cesare, B., Gómez-Pugnaire, M. T. & Rubatto, D. (2003). Residence time of S-type anatectic magmas beneath the Neogene Volcanic Province of SE Spain: a zircon and monazite SHRIMP study. *Contributions to Mineralogy and Petrology* **146**, 28–43.

Cesare, B., Meli, S., Nodari, L. & Russo, U. (2005). Fe^{+3} reduction during biotite melting in graphite metapelites: another origin of CO_2 in granulites. *Contributions to Mineralogy and Petrology* **149**, 129–140.

Cesare, B., Rubatto, D. & Gómez-Pugnaire, M. T. (2009*a*). Do extrusion ages reflect magma generation processes at depth? An example from the Neogene Volcanic Province of SE Spain. *Contributions to Mineralogy and Petrology* **157**, 267–279.

Cesare, B., Ferrero, S., Salvioli-Mariani, E., Pedron, D. & Cavallo, A. (2009*b*). 'Nanogranite' and glassy inclusions: the anatectic melt in migmatites and granulites. *Geology* **37**, 627–630.

Chappell, B.W. (1999). Aluminum saturation in I- and S-type granites and the characterization of fractionated haplogranites. *Lithos* **46**, 535–551.

Clemens, J. D. & Watkins, J. M. (2001). The fluid regime of high-temperature metamorphism during granitoid magma genesis. *Contributions to Mineralogy and Petrology* **140**, 600–606.

Connolly, J. A. D. & Cesare, B. (1993). C-O-H-S fluid composition and oxygen fugacity in graphitic metapelites. *Journal of Metamorphic Geology* **11**, 379–388.

Duggen, S., Hoernle, K., Van der Bogaard, P. & Garbe-Schönberg, D. (2005). Post-collisional transition from subduction- to intraplate-type magmatism: evidence from continental-edge delamination of subcontinental lithosphere. *Journal of Petrology* **46**, 1155–1201.

Eggins, S. M. (2003). Laser ablation ICP-MS of geological materials prepared as Lithium Borate glasses. *Geostandards Newsletter* **27**, 147–162.

Eggins, S. M., Rudnick, R. L. & McDonough, W. F. (1998). The composition of peridotites and their minerals: a laser ablation ICP-MS study. *Earth and Planetary Science Letters* **154**, 53–71.

Evenson, J. M. & London, D. (2003). Experimental silicate mineral/melt partition coefficients for beryllium and the crustal Be cycle from migmatite to pegmatite. *Geochimica et Cosmochimica Acta* **66**, 2239–2265.

Fernández-Soler, J. M., Acosta-Vigil, A., Gómez-Pugnaire, M. T. & Comas, M. C. (2007). Magma mixing in El Hoyazo volcanics, Betic Cordilleras (SE Spain). *Geophysical Research Abstracts* **9**, 04202.

Frezzotti, M. L., Peccerillo, A., Zanon, V. & Nikogosian, I. (2004). Silica-rich melts in quartz xenoliths from Vulcano Island and their

bearing on processes of crustal anatexis and crust–mantle interaction beneath the Aeolian Arc, southern Italy. *Journal of Petrology* **45**, 3–26.

Grant, J. A. (1985). Phase equilibria in low-pressure partial melting of pelitic rocks. *American Journal of Science* **285**, 409–435.

Gregory, C. J., Buick, I. S., Hermann, J. & Rubatto, D. (2009). Mineral-scale trace element and U–Th–Pb age constraints on metamorphism and melting during the Petermann orogeny (central Australia). *Journal of Petrology* **50**, 251–287.

Gromet, L. P., Dymek, R. F., Haskin, L. A. & Korotev, R. L. (1984). The 'North American shale composite': its compilation, major and trace element characteristics. *Geochimica et Cosmochimica Acta* **48**, 2469–2482.

Harris, N., Ayres, M. & Massey, J. (1995). Geochemistry of granitic melts produced during the incongruent melting of muscovite: implications for the extraction of Himalayan leucogranite magmas. *Journal of Geophysical Research* **100**, 15767–15777.

Harrison, T. M. & Watson, E. B. (1983). Kinetics of zircon dissolution and zirconium diffusion in granitic melts of variable water content. *Contributions to Mineralogy and Petrology* **84**, 66–72.

Henderson, P., Nolan, J., Cunningham, G. C. & Lowry, R. K. (1985). Structural controls and mechanisms of diffusion in natural silicate melts. *Contributions to Mineralogy and Petrology* **89**, 263–272.

Hermann, J. & Rubatto, D. (2003). Relating zircon and monazite domains to garnet growth zones: age and duration of granulite facies metamorphism in the Val Malenco lower crust. *Journal of Metamorphic Geology* **21**, 833–852.

Holness, M. B. & Sawyer, E. W. (2008). On the pseudomorphing of melt-filled pores during the crystallization of migmatites. *Journal of Petrology* **49**, 1343–1363.

Holtz, F. & Johannes, W. (1994). Maximum and minimum water contents of granitic melts: implications for chemical and physical properties of ascending magmas. *Lithos* **32**, 149–159.

Holtz, F., Johannes, W., Tamic, N. & Behrens, H. (2001). Maximum and minimum water contents of granitic melts generated in the crust: a reevaluation and implications. *Lithos* **56**, 1–14.

Huang, W. L. & Wyllie, P. J. (1981). Phase relationships of S-type granite with H_2O to 35 kbar: muscovite granite from Harney Peak, South Dakota. *Journal of Geophysical Research* **86**, 10515–10529.

Icenhower, J. & London, D. (1995). An experimental study of element partitioning among biotite, muscovite, and coexisting peraluminous silicic melt at 200 MPa (H_2O). *American Mineralogist* **80**, 1229–1251.

Johannes, W. & Holtz, F. (1992). Melting of plagioclase in granite and related systems: composition of coexisting phases and kinetic observations. *Transactions of the Royal Society of Edinburgh: Earth Sciences* **83**, 417–422.

Jung, S. & Hellebrand, E. (2006). Trace element fractionation during high-grade metamorphism and crustal melting—constraints from ion microprobe data of metapelitic, migmatitic and igneous garnets and implications for Sm–Nd garnet chronology. *Lithos* **87**, 193–213.

Kosler, J. (2001). Laser-ablation ICPMS study of metamorphic minerals and processes. In: Sylvester, P. (ed.) *Laser-Ablation-ICPMS in the Earth Sciences. Principles and Applications. Mineralogical Society of Canada, Short Course* **29**, 185–202.

Kretz, R. (1983). Symbols for rock-forming minerals. *American Mineralogist* **68**, 277–279.

Le Breton, N. & Thompson, A. B. (1988). Fluid-absent (dehydration) melting of biotite in metapelites in the early stages of crustal anatexis. *Contributions to Mineralogy and Petrology* **99**, 226–237.

López Ruiz, J. & Rodríguez Badiola, E. (1980). La región volcánica Neógena del sureste de España. *Estudios Geológicos* **36**, 5–63.

Miller, C. F., Hanchar, J. M., Wooden, J. L., Bennett, V. C., Harrison, T. M., Wark, D. A. & Foster, D. A. (1992). Source region of a granite batholith: evidence from lower crustal xenoliths and inherited accessory minerals. *Transactions of the Royal Society of Edinburgh: Earth Sciences* **83**, 49–62.

Montel, J. M. (1993). A model for monazite/melt equilibrium and applications to the generation of granitic magmas. *Chemical Geology* **110**, 127–146.

Mungall, J. E., Dingwell, D. B. & Chaussidon, M. (1999). Chemical diffusivities of 18 trace elements in granitoid melts. *Geochimica et Cosmochimica Acta* **63**, 2599–2610.

Munksgaard, N. C. (1984). High $\delta^{18}O$ and possible pre-eruptional Rb–Sr isochrons in cordierite-bearing Neogene volcanics from SE Spain. *Contributions to Mineralogy and Petrology* **87**, 351–358.

Muñoz-Espadas, M. J., Lunar, R. & Martínez-Frías, J. (2000). The garnet placer deposit from SE Spain: indrustrial recovery and geochemical features. *Episodes* **23**, 266–269.

Norman, M. D., Griffin, W. L., Pearson, N. J., Garcia, M. O. & O'Reilly, S. Y. (1998). Quantitative analysis of trace element abundances in glasses and minerals: a comparison of laser ablation inductively coupled plasma mass spectrometry, solution inductively coupled plasma mass spectrometry, proton microprobe and electron microprobe data. *Journal of Analytical Atomic Spetrometry* **13**, 477–482.

Patiño Douce, A. E. & Harris, N. (1998). Experimental constraints on Himalayan anatexis. *Journal of Petrology* **39**, 689–710.

Patiño Douce, A. E. & Johnston, A. D. (1991). Phase equilibria and melt productivity in the pelitic system: implications for the origin of peraluminous granitoids and aluminous granulites. *Contributions to Mineralogy and Petrology* **107**, 202–218.

Pattison, D. R. M. (1992). Stability of andalusite and sillimanite and the Al_2SiO_5 triple point, constraints from the Ballachulish aureole, Scotland. *Journal of Geology* **100**, 423–446.

Pearce, N. J. G., Perkins, W. T., Westgate, J. A., Gorton, M. P., Jackson, S. E., Neal, C. R. & Chenery, S. P. (1997). A compilation of new and published major and trace element data for NIST SRM 610 and NIST SRM 612 glass reference materials. *Geostandard Newsletter* **21**, 115–144.

Perini, G., Cesare, B., Gómez-Pugnaire, M. T., Ghezzi, L. & Tommasini, S. (2009). Armouring effect on Sr–Nd isotopes during disequilibrium crustal melting: the case study of frozen migmatites from El Hoyazo and Mazarrón, SE Spain. *European Journal of Mineralogy* **21**, 117–131.

Peto, P. (1976). An experimental investigation of melting relationships involving muscovite and paragonite in the silica-saturated portion of the system K_2O–Na_2O–Al_2O_3–SiO_2–H_2O to 15 kbar total pressure. In: *Progress in Experimental Petrology*, 3rd Report. London: NERC, pp. 41–45.

Pickering, J. & Johnston, A. D. (1998). Fluid-absent melting behavior of a two-mica metapelite: experimental constraints on the origin of Black Hills granite. *Journal of Petrology* **39**, 1787–1804.

Reid, M. R. (1990). Ionprobe investigation of rare earth element distributions and partial melting of metasedimentary granulites. In: Vielzeuf, D. & Vidal, Ph. (eds) *Granulites and Crustal Evolution*. Dordrecht: Kluwer, pp. 507–522.

Roedder, E. (ed.) (1984). *American Mineralogist, Reviews in Mineralogy* **12**, 644.

Rubatto, D., Hermann, J. & Buick, I. S. (2006). Temperature and bulk composition control on the growth of monazite and zircon during low-pressure anatexis (Mount Stafford, Central Australia). *Journal of Petrology* **47**, 1973–1996.

Sawyer, E. W. (1991). Disequilibrium melting and the rate of melt–residuum separation during migmatization of mafic rocks from the Grenville Front, Quebec. *Journal of Petrology* **32**, 701–738.

Sawyer, E. W. (1994). Melt segregation in the continental crust. *Geology* **22**, 1019–1022.

Silva, M. M. V. G. & Neiva, A. M. R. (1990). Geochemistry of the granites and their minerals from Paredes da Beira–Penedono, northern Portugal. *Chemical Geology* **85**, 147–170.

Sun, S. S. & McDonough, W. F. (1989). Chemical and isotopic systematics of oceanic basalts: implications for mantle composition and processes. In: Saunders, A. D. & Norry, M. J. (eds) *Magmatism in the Ocean Basins*. Geological Society, London, Special Publications **42**, 313–345.

Tajcmanová, L., Connolly, J. A. D. & Cesare, B. (2009). A thermodynamic model for titanium and ferric iron solution in biotite. *Journal of Metamorphic Geology* **27**, 153–165.

Taylor, S. R. & McLennan, S. M. (1985). *The Continental Crust: its Composition and Evolution*. Oxford: Blackwell Scientific, 312 pp.

Thompson, A. B. (1982). Dehydration melting of pelitic rocks and the generation of H_2O-undersaturated granitic liquids. *American Journal of Science* **282**, 1567–1595.

Tuttle, O. F. & Bowen, N. L. (1958). *Origin of granite in the light of experimental studies in the system $NaAlSi_3O_8$–$KAlSi_3O_8$–SiO_2–H_2O. Geological Society of America, Memoirs* 74.

Vielzeuf, D. & Holloway, J. R. (1988). Experimental determination of the fluid-absent melting relations in the pelitic system. *Contributions to Mineralogy and Petrology* **98**, 257–276.

Vielzeuf, D., Clemens, J. D., Pin, C. & Moinet, E. (1990). Granites, granulites and crustal differentiation. In: Vielzeuf, D. & Vidal, Ph. (eds) *Granulites and Crustal Evolution*. Dordrecht: Kluwer, pp. 59–85.

Watson, E. B. & Harrison, T. M. (1984). Accessory minerals and the geochemical evolution of crustal magmatic systems: a summary and prospectus of experimental approaches. *Physics of the Earth and Planetary Interiors* **35**, 19–30.

Watson, E. B., Vicenzi, E. P. & Rapp, R. P. (1989). Inclusion/host relations involving accessory minerals in high-grade metamorphic and anatectic rocks. *Contributions to Mineralogy and Petrology* **101**, 220–231.

Yardley, B. D. (1989). *An Introduction to Metamorphic Petrology*. Harlow: Longman, 248 pp.

Zeck, H. P. (1968). Anatectic origin and further petrogenesis of almandine-bearing biotite–cordierite–labradorite-dacite with many inclusions of restite and basaltoid material, Cerro del Hoyazo, SE Spain. PhD thesis, Amsterdam University, Holland, 161 pp.

Zeck, H. P. (1970). An erupted migmatite from Cerro del Hoyazo, SE Spain. *Contributions to Mineralogy and Petrology* **26**, 225–246.

Zeck, H. P. (1992). Restite–melt and mafic–felsic magma mingling in an S-type dacite, Cerro del Hoyazo, southeastern Spain. *Transactions of the Royal Society of Edinburgh: Earth Sciences* **83**, 139–144.

Zeck, H. P. & Williams, I. (2002). Inherited and magmatic zircon from Neogene Hoyazo cordierite dacite, SE Spain—anatectic source rock provenance and magmatic evolution. *Journal of Petrology* **43**, 1089–1104.